Sofia University "St. Kl. Ohridski"

Faculty of Physics
Atomic Physics Dept.

Bachelor thesis

Probing the antimatter in the Universe

Veronika Asova

Nuclear and Particle Physics, Faculty number: № 0PH0760004

Supervisor:
Dr. Radoslav Simeonov

Co-supervisor:
Assoc. prof. Dr. Venelin Kozhuharov

Sofia, 10 September 2025

Contents

Chapter 1

Introduction

Perhaps the most obscure and curious topic in particle physics is the nature of antimatter. The idea that atoms have a counterpart, with which they annihilate and release energy, has been troubling scientists since the 1928 [1]. That is when Paul Dirac first predicted the existence of antimatter [1] - a concept that was experimentally confirmed with the discovery of the positron by Carl Anderson in 1932 [2]. Even before physics was formalized as a field, people sought to understand the underlying principles of our universe. One example comes from Hermetic philosophy, where the fourth principle, known as the Principle of Polarity, states: "Everything is dual; everything has poles; everything has its pair of opposites; like and unlike are the same; opposites are identical in nature but different in degree; extremes meet; all truths are but half-truths; all paradoxes may be reconciled." (The Kybalion, 1908). While not scientific, this ancient idea of duality interestingly parallels the modern concept of matter and antimatter — two entities identical in many respects, yet fundamentally opposite.

1.1 First indication of anti-matter existence

1.1.1 Historical overview

Everything started in 1905, when Albert Einstein published his paper "Zur Elektrodynamik bewegter Körper", which introduced his theory of special relativity [3, 4]. He emphasises on the dependence between energy and mass and on the relationship between space and time, using Planck's energy quanta to describe how light travels through space. His work set the framework in which relativistic quantum mechanics was later needed [4].

Coming back to Planck's energy quanta, in the 1920s Erwin Schrödinger and Werner Heisenberg developed a new, nonrelativistic quantum theory. It works well for particles moving slowly, but not for particles moving close to the speed of light. Paul Dirac, seeing the need to combine quantum mechanics with special relativity, derived an equation to describe an electron moving at relativistic speed [1, 4]. The main difference between the Dirac equation and the Schrödinger's equation is that Schrödinger build his wave equation using the Newtonian energy formula combined with the de Broglie's relations to get the time-dependent wave equation. Dirac used Einstein's relativistic energy-momentum relation. But there was a huge problem. When solved, the equation gives four independent solutions - two with positive energy and two with negative energy. The positive energy solutions correspond to electrons and to what Dirac expected, but the negative energy solutions implied the existence of unbounded energy states that can make the electrons undergo spontaneous transitions to lower and lower energy states. This could make the electrons release infinite energy. [5, 6, 4].

If these states were real, there would be nothing stopping electrons from falling into these energy states, considering every system's tendency to move to a lower energy state. This would make the vacuum unstable. At first, Dirac tried to disregard the negative solutions, but he realized that if he were to do that, his entire mathematical foundation would collapse. Then, he came up with an idea to explain this anomaly. He proposed the idea of a "Dirac Sea", which suggests that all negative energy states are already filled in the vacuum. He applied the Pauli exclusion principle, which states that no two electrons can occupy the same state. Suppose there is a hole in the negative energy states - that Dirac suggest is positively charged electron or in other words - a positron [5].

In 1932 Carl Anderson studied cosmic rays using a Wilson cloud chamber which was filled with supersaturated vapor [2]. When a charged particle passes through it ionizes the gas. When this happens the vapor condenses along its path and leaves a visible track of the particle's trajectory, as shown in Fig. 1.1. Adding a magnetic field perpendicular to the chamber allowed him to observe the particle's momentum and charge. The direction of the curvature along the track (left or right bend) determines the charge sign and the radius of the curvature determines its momentum [2]. Anderson then made a strange observation - he noticed tracks from cosmic rays that curved into the opposite direction of the electrons. This meant that they have positive charge. The curvature also showed that they have a mass close to the ones of the electrons, so it couldn't have been a proton. To determine the type of the particle he placed a thin lead plate inside the chamber. That officially excluded the possibility for protons. He concluded that it was a positively charged electron - a positron [1]. The particle that Dirac had predicted. He published his discoveries in Science (1932) - "The Positive Electron" [2]. This paper earned him a Nobel Prize in 1936 [4]. And that is how the first antimatter particle was discovered and paved the way to scientific progress.

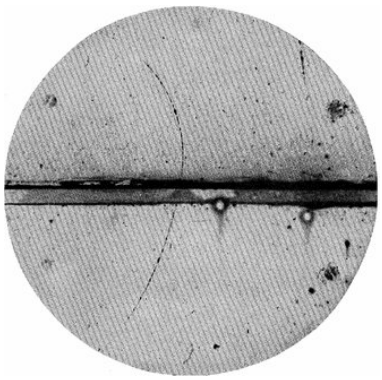

Figure 1.1: Cloud-chamber photograph of the first observed positron [2].

Chapter 2

Matter-antimatter problem of the Universe

2.1 The Dirac Equation

The Dirac equation is a crucial milestone for understanding the nature of antimatter. It yields four solutions - two positive-energy and two negative-energy states. We begin with the simplest limit: the rest-frame (stationary) solution of the Dirac equation.

2.1.1 Solving the Dirac Equation

The Dirac equation in its full form is written as:

$$i\hbar\frac{\partial\psi}{\partial t} = \left(-i\hbar c\boldsymbol{\alpha}\cdot\nabla + \beta mc^2\right)\psi \tag{2.1}$$

Here, ψ is not a wavefunction like in non-relativistic quantum mechanics, but a four-component object called a Dirac spinor. It has four components stacked together. The matrices $\alpha = (\alpha_x, \alpha_y, \alpha_z)$ and β are 4×4 matrices that mix these components in a specific way to ensure the equation is consistent with relativity [1, 5].

Now, if the particle is stationary, its momentum is equal to 0. In quantum mechanics, the momentum p is represented by the differential operator:

$$p = -i\hbar\nabla \tag{2.2}$$

The term $-i\hbar c\alpha\cdot\nabla$ in the Dirac equation is essentially the momentum operator acting on the wavefunction ψ. This means the term involving the momentum disappears because it is multiplied by zero. Then the equation simplifies to:

$$i\hbar\frac{\partial\psi}{\partial t} = \beta mc^2\psi \tag{2.3}$$

The equation 2.3 is a much simpler equation to work with. It tells us that the time evolution of the particle's wavefunction is determined only by its rest mass energy (mc^2) and the β matrix [6].

1. Solving the Simplified Equation

   Since the particle is stationary, we can assume the wavefunction has a simple time dependence:

$$\psi(t) = u\, e^{-iEt/\hbar} \tag{2.4}$$

In 2.4, u is a four-component spinor that does not depend on time, and E is the energy of the particle. Substituting this into the simplified Dirac equation gives:

$$Eu = \beta mc^2 u \tag{2.5}$$

If we assume $m \neq 0$ and divide both sides by mc^2, we get:

$$\beta u = \left(\frac{E}{mc^2}\right) u \tag{2.6}$$

And just like that, we got the eigenvalue equation. In equation 2.6 β is a matrix, u is an eigenvector, and

$$E/mc^2$$

is the eigenvalue. In setting up the equation, Dirac choose the matrix β so that squaring the equation gives Einstein's relativistic relation $E^2 = p^2c^2 + m^2c^4$ [1]. This works only if β multiplied by itself gives the identity matrix $\beta^2 = I$.

From this property, it follows that the possible eigenvalues of β are $+1$ or -1. This leads to the two energy solutions $E = \pm mc^2$ [5].

2. The Structure of the β Matrix and Its Eigenvalues

In the Dirac equation 2.1 the term βmc^2 stands for the rest mass energy of the particle. Without it, the equation would describe massless particles, like photons. The β matrix is given in its standard form as:

$$\beta = \begin{pmatrix} I_2 & 0 \\ 0 & -I_2 \end{pmatrix} \tag{2.7}$$

where I_2 is the 2×2 identity matrix. If we write it out fully, it becomes:

$$\beta = \begin{pmatrix} 1 & 0 & 0 & 0 \\ 0 & 1 & 0 & 0 \\ 0 & 0 & -1 & 0 \\ 0 & 0 & 0 & -1 \end{pmatrix} \tag{2.8}$$

The matrix 2.8 is diagonal. This means that its eigenvalues are simply the entries on the diagonal. This immediately tells us that the possible values for $\frac{E}{mc^2}$ are $+1$ and -1. It means that:

- If $\frac{E}{mc^2} = +1$, then $E = +mc^2$ (positive energy).
- If $\frac{E}{mc^2} = -1$, then $E = -mc^2$ (negative energy).

The β matrix naturally splits the 4-component Dirac spinor ψ into upper (ψ_A) and lower (ψ_B) 2-component spinors [5]:

$$\psi = \begin{pmatrix} \psi_A \\ \psi_B \end{pmatrix}, \quad \psi_A = \begin{pmatrix} \psi_1 \\ \psi_2 \end{pmatrix}, \quad \psi_B = \begin{pmatrix} \psi_3 \\ \psi_4 \end{pmatrix}. \tag{2.9}$$

- For positive-energy solutions ($E = +mc^2$): $\psi_B = 0$
- For negative-energy solutions ($E = -mc^2$): $\psi_A = 0$

3. Finding the Eigenvectors (Spinor Solutions)

   Now, we need to find the actual spinors u that correspond to our eigenvalues of $+1$ and -1. We have two cases [6, 5]:

   - Case 1: Positive Energy Solutions ($E = +mc^2$)

   For eigenvalue $\lambda = +1$, the eigenvalue equation $\beta u = +u$ becomes:

$$\begin{pmatrix} I_2 & 0 \\ 0 & -I_2 \end{pmatrix} \begin{pmatrix} u_A \\ u_B \end{pmatrix} = + \begin{pmatrix} u_A \\ u_B \end{pmatrix} \tag{2.10}$$

   This splits into two separate equations:

   (a) $u_A = +u_A$ (which is always true, so u_A is arbitrary).

   (b) $-u_B = +u_B$ (which implies $u_B = 0$).

   Then, the general solution for positive energy is:

$$u_+ = \begin{pmatrix} u_A \\ 0 \end{pmatrix} = \begin{pmatrix} \psi_1 \\ \psi_2 \\ 0 \\ 0 \end{pmatrix} \tag{2.11}$$

   In 2.11 we can see that ψ_1 and ψ_2 are arbitrary complex numbers. They represent the two possible spin states of the particle. Like spin-up and spin-down for an electron.

   - Case 2: Negative Energy Solutions ($E = -mc^2$)

   For $\lambda = -1$, the equation $\beta u = -u$ becomes:

$$\begin{pmatrix} I_2 & 0 \\ 0 & -I_2 \end{pmatrix} \begin{pmatrix} u_A \\ u_B \end{pmatrix} = - \begin{pmatrix} u_A \\ u_B \end{pmatrix} \tag{2.12}$$

   Again, this splits into two equations:

   (a) $u_A = -u_A$ (which implies $u_A = 0$).

   (b) $-u_B = -u_B$ (which is always true, so u_B is arbitrary).

   Then, the general solution for negative energy is:

$$u_- = \begin{pmatrix} 0 \\ u_B \end{pmatrix} = \begin{pmatrix} 0 \\ 0 \\ \psi_3 \\ \psi_4 \end{pmatrix} \tag{2.13}$$

   In 2.13 ψ_3 and ψ_4 are arbitrary complex numbers representing the spin states of the negative-energy solution [6].

2.1.2 Interpretation of the Solutions

The positive energy states describe ordinary particles (like electrons) at rest. The two components ϕ_1 and ϕ_2 correspond to the two possible spin states (up and down) [6]. On the other hand, negative energy states seem unreal, especially if they are compared to classical physics, where energy is always positive. If particles could have negative energy, they would keep falling into lower and lower energy states, releasing infinite energy, which is not what we observe [6]. As it was mentioned in the introduction, Dirac proposed that all negative energy states are already filled, forming a "sea" of particles. The Dirac sea is visually represented in Fig 2.1, where a hole would behave like a particle with positive energy and opposite charge - an antiparticle [1, 5].

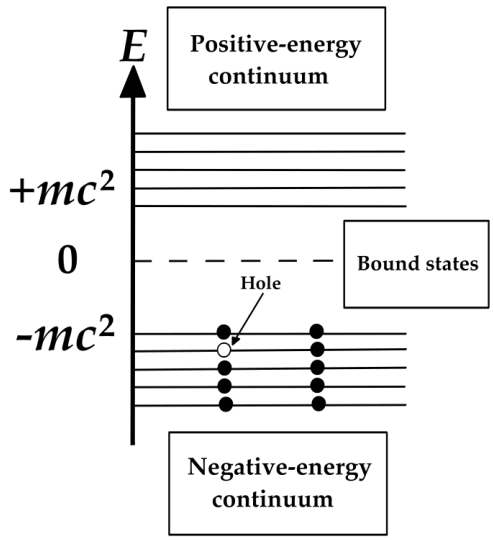

Figure 2.1: Visual representation of the Dirac Sea

Feynman studied the problem of negative-energy solutions in the Dirac equation [7]. He proposed that these solutions could be understood in a new way. Instead of treating them as electrons with impossible energies, he saw them as particles with positive energy moving backward in time or antiparticles moving forward in time. In this view, a negative-energy electron is the same as a positron. The positron can also be described as an electron moving backward in time in the mathematics, but in reality it moves forward like any other particle [7].

1. **Consistency with the energy-momentum relation.**
   The Dirac equation is constructed as a "square root" of Einstein's relativistic relation,

$$E^2 = p^2c^2 + m^2c^4.$$

   Just as the quadratic equation $x^2 = 4$ necessarily has two solutions, $x = \pm 2$, the relativistic energy relation has both positive and negative solutions,

$$E = \pm\sqrt{p^2c^2 + m^2c^4}.$$

When Dirac linearized this expression to obtain a first-order equation in both time and space, both signs naturally appeared. To remove the negative solutions by hand would be mathematically inconsistent with the structure of the relativistic theory. The presence of both branches is not an accident, but a direct consequence of combining quantum mechanics with special relativity [6].

2. **Lorentz invariance.**
   Another essential reason is the requirement of Lorentz invariance. If we were to discard the negative-energy solutions, the set of allowed states would no longer transform properly under Lorentz transformations. In other words, an observer moving in a different inertial frame might see a solution that appears positive in one frame but negative in another. Restricting the solutions to only the positive solutions would undermine the relativistic symmetry of the equation, thus making it inconsistent with the requirements of special relativity [5].

3. **Physical reality of antiparticles.**
   Finally, and perhaps most convincingly, nature itself makes use of the negative-energy solutions. When Dirac first encountered them, he interpreted them through his famous "hole theory", which predicted the existence of antiparticles. The prediction was confirmed only a few years later by Anderson's discovery of the positron in cosmic ray experiments. Today, antiparticles are an established part of particle physics. Thus, the negative-energy branch is not something that can be discarded. It corresponds directly to real particles that have been experimentally observed [1, 2].

In short, the negative-energy solutions of the Dirac equation are not a nuisance to be ignored, but an indispensable part of a consistent relativistic quantum theory. They are demanded both by the mathematics of the equation and by the physical reality of the universe.

2.1.3 Probability Density and Consistency

In quantum mechanics, the probability density shows where a particle is most likely to be found. Probabilities, by definition, lie in 0,1 — a negative chance doesn't exist. This becomes an important issue when we try to combine quantum mechanics with Einstein's relativity [5].

The Klein-Gordon equation was the first major attempt to build a relativistic quantum theory. It works well for spin-0 particles like pions, but it has a serious drawback: for some solutions, the probability density can turn negative. This happens because the equation is second order in time, so the density depends both on the wavefunction and on its time derivative. In certain cases, this combination gives a negative result — something that is physically absurd, like claiming an electron has a "-20% chance" of being somewhere [6, 5].

Dirac saw that the problem lay in the form of the equation itself. His solution was to create a first-order equation, now known as the Dirac equation, which avoids this difficulty entirely. By using four-component spinors, the probability density becomes [1]:

$$\rho = \psi^\dagger \psi = |\psi_1|^2 + |\psi_2|^2 + |\psi_3|^2 + |\psi_4|^2,$$

This expression is always positive because it's a sum of squared magnitudes. Dirac's approach solved the probability issue, naturally included spin, and predicted the existence of antimatter [5]. The Klein–Gordon equation is useful for bosons, but in quantum field theory their probability interpretation is handled differently [6].

2.2 Standard Model and matter-antimatter symmetry

Matter and antimatter are expected to behave in the same way. Afterall, the Standard Model (SM) and quantum field theory state that the laws of physics should treat matter and antimatter identically [5, 8]. They are the same when we convert all the charges and reverse the spatial coordinates. When the universe began with the Big Bang, it should have created equal amounts of matter and antimatter [9, 4]. One particle of matter and one of antimatter for every reaction. That would result in equal ratio of protons to antiprotons, electrons to positrons and neutrons to antineutrons. Then, when they interact, they would annihilate, releasing energy in the process [10].

$$e^- + e^+ \rightarrow 2\gamma$$

$$p + \overline{p} \rightarrow \pi^+ + \pi^- + \pi^0$$

The neutral pions (π^0) decay almost instantly into gamma rays, having a lifetime of 8.4×10^{-17} s [5]. Matter–antimatter annihilation converts rest mass into high-energy photons, mostly gamma rays. If matter and antimatter had been created in equal amounts, they would have annihilated almost completely. This would have left the universe filled only with radiation - without atoms, stars, galaxies, or people [9]. Observationally, we see a matter-dominated universe. No anti-galaxies or anti-stars are detected, which poses the question: where did the antimatter go?

2.3 CP violation and proton decay

Many of the main principles in physics are directly linked to symmetry. Symmetries in physics represent transformations under which the laws of nature remain invariant. Noether's theorem establishes a correspondence between continuous symmetries and conservation laws: invariance under time transformations leads to energy conservation, invariance under spatial transformations to momentum conservation, and gauge invariance to charge conservation[5, 8, 11].

Physicists once treated the discrete symmetries parity (P), charge conjugation (C), and their product (CP) as exact, using them to classify particles and interactions[9, 5]. CP symmetry is a combination of two symmetries: C and P symmetry. Charge conjugation symmetry states that particles should have the same physical properties if we convert their charge, baryon number, lepton number, etc. P symmetry states that if we mirror the spatial coordinates of a system, the physical properties would remain the same. In other words, if we convert the sign of all spatial coordinates (x -> -x, y -> -y, z -> -z), the physics shouldn't change [12, 5].

CP violation means that if we upend particles with antiparticles and mirror the system, the resulting interaction is not identical to the original. This was firstly observed in the decay of neutral kaons by Christenson, Cronin, Fitch and Turlay [13, 14]. They were studying neutral kaons at the Brookhaven National Laboratory, where they observed K^0 particles by colliding protons to a beryllium target. Their experimental setup is shown on Fig. 2.2. The kaon beam traveled through a chamber, filled with helium. The distance from the target to the helium-filled decay region was chosen so that the short-lived component ($K_S \approx K_1^0$) decayed before entering the chamber, leaving a predominantly long-lived K_L ($\approx K_2^0$) beam there. According to the theory back then, long-lived K_2^0 particles should never decay into two pions ($\pi^+\pi^-$). That's because K_2^0 was considered CP-odd while two-pion states are CP-even. CP-even means that the wavefunction describing a system stays identical when particles

are swapped with antiparticles and mirror it, while CP-odd means it changes sign under the same transformation. To confirm these are really two-pion decays, they used a spark chamber. It is a detector that makes charged particles visible as electric sparks, which allows precise measurement of their paths. Out of 23,000 observed K_2^0 decays, they found 45 cases (0.2 %) where the kaon decayed into two pions, instead of three [13].

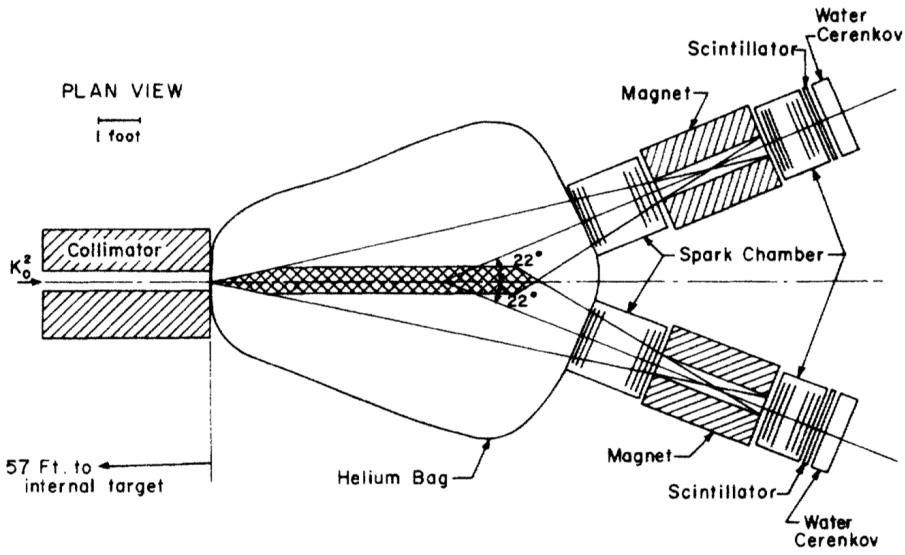

Figure 2.2: The experimental setup used to discover the CP violation in the neutral kaon system. [14]

As a charged particle passes through the spark chamber, it ionizes the gas by knocking electrons off the atoms. A high voltage is applied across two parallel metal plates. That way, the free electrons will lower the breakdown voltage where ionization has occurred. This creates a spark along the ionization's track, which is captured by cameras. In the scintillator, the pion excites molecules in a scintillation material, which then release light. This light is detected by a photomultiplier tube (PMT), which converts it into an electrical signal. The Water Cherenkov detector is used to identify and confirm the particle. If the particle moves faster than the speed of light in water, it emits a cone of blue Cherenkov light. Then it is also picked up by the PMTs. By detecting this light, we can confirm that the particle is moving fast enough to be a pion. This cancels the possibility of a heavier, slower particle like a proton [10, 5].

This is a small but undeniable violation of CP symmetry. Their research won them a Nobel Prize in 1964 [14]. Later, CP violation was also confirmed in B-meson decays [15]. But we can go even deeper and dive into the fundamental reason for CP violation - Weak force.

2.3.1 Weak interaction and proton decay

The weak interaction is one of the four fundamental forces. The others are gravity, electromagnetism, and the strong interaction. What makes the weak force different is that it can change the flavor of quarks and leptons. Because of this, it is responsible for processes such as beta decay and neutrino scattering. On the quark level, beta decay happens when a down quark turns into an up quark. This occurs through the emission of a virtual W^- boson. The W^- then decays into an electron and an electron antineutrino.

The weak interaction also breaks fundamental symmetries. P violation was first shown in nuclear beta decay by Wu and collaborators in 1957 [12]. CP violation was later discovered in neutral kaon decays by Christenson, Cronin, Fitch, and Turlay in 1964 [13]. In the SM,

these effects are explained by the fact that quarks of different flavors mix with each other. This idea was introduced by Kobayashi and Maskawa [16]. Another important feature of the weak interaction is its short range. It acts over distances of about 10^{-18} m [17]. This is due to the large masses of the mediating $W^{\pm}$ and Z^0 bosons [10, 5]. Unlike electromagnetism and gravity, which act over larger distances, the weak force is confined to subnuclear scales. These properties make the weak interaction essential for understanding particle physics and also processes in the early universe.

The weak force is carried by three particles: the W^+, W^-, and Z^0 bosons. All of them are much heavier than the proton, with masses between about 80 and ~ 91GeV [17]. Their large mass restricts the weak interaction to very short distances, about 10^{-18} m [17]. Because of this short range, the weak force is less relevant than the electromagnetic or strong interactions in low-energy processes. At high energies, however, its strength becomes comparable to electromagnetism. This behavior reflects their common origin in the electroweak theory [10, 5].

A distinctive feature of the weak interaction is that it is chiral, meaning it treats particles differently depending on the orientation of their spin relative to their momentum. In particle physics, this orientation is called handedness helicity for massless particles.

A left-handed particle is one where the spin direction is opposite to the direction of motion. A right-handed particle has its spin pointing in the same direction as its motion. For antiparticles, the definition reverses: a right-handed antiparticle has spin opposite to its motion, and a left-handed antiparticle has spin aligned with its motion.

In the SM, the charged weak interaction is mediated by the $W^{\pm}$ bosons. It couples only to left-handed particles and right-handed antiparticles. Right-handed particles and left-handed antiparticles do not experience the W-mediated weak force at all. This property is built into the electroweak theory [11, 5].

As noted above, the charged weak interaction acts only on left-handed fermions (and right-handed antifermions), which is why parity is maximally violated. This was established in 1957 by Chien-Shiung Wu, who demonstrated that electrons from beta decay are emitted preferentially in one direction relative to the spin of the decaying nucleus [12]. Later studies also established that the weak force violates CP symmetry, first observed in kaon decays [13]. Together, these results demonstrate that the weak interaction is fundamentally different from the strong and electromagnetic forces.

The neutral weak interaction mediated by the Z^0 boson is slightly different. It couples to both left- and right-handed particles, but with different strengths. That means parity is not conserved [17]. The reason for this asymmetry lies in the way SM unifies the weak and electromagnetic forces. The theory is based on the gauge group $SU(2)_L \times U(1)_Y$, where the "L" in $SU(2)_L$ stands for "left-handed." Only left-handed fermions are placed into weak isospin doublets. Those are pairs of particles such as (ν_e, e^-) or (u, d). Right-handed fermions are singlets under $SU(2)_L$, meaning they do not participate in the charged weak interaction. This structure is not arbitrary: it is the only arrangement that makes the theory mathematically consistent, renormalizable, and able to match experimental observations [11, 5, 8].

This handedness structure is deeply connected to CP violation. Since only certain spin states are allowed to interact, the rules for transforming particles into their antiparticles (C) and swapping spatial coordinates (P) do not lead back to the same physics. This imbalance between matter and antimatter behavior is one of the Sakharov conditions needed to generate the matter-antimatter asymmetry in the Universe. Sakharov identified three requirements: baryon number violation, C and CP violation, and a departure from thermal equilibrium [16, 18].

As for proton decay – the chirality of the weak interaction itself does not directly cause it. In the SM, baryon number is conserved, and the proton is stable [10, 5]. However, many

Grand Unified Theories (GUTs) extend the SM's gauge group to something larger, such as $SU(5)$ or $SO(10)$, where quarks and leptons are part of the same multiplets [19]. In these theories, there are new heavy gauge bosons (often called X and Y) that can convert quarks into leptons. Because quarks make up protons, these interactions can lead to the proton decaying into lighter particles like a positron and a neutral pion.

Although proton decay has never been observed, its search is motivated partly by the same unification ideas that explain why the weak force has its chiral structure [11, 8]. If such a unification is correct, the very mechanism that ties quarks and leptons together could also allow rare processes that violate baryon number – and thus cause protons to decay.

Chapter 3

Antimatter in space

The milestone to study antimatter in space are the cosmic rays. Most of the antimatter detection is thought to be secondary — created when fast cosmic rays collide with clouds of interstellar gas [20]. These are usually protons hitting hydrogen or helium. In those high-energy impacts, new particles are formed, and among them are antiprotons and positrons. If we know how cosmic rays travel through the Galaxy and how much interstellar gas they hit on the way, then we can calculate how many antiprotons and positrons they should produce, and what energies those particles will have [21].

If the only source of antimatter was these secondary collisions, the measured flux should follow a well-known pattern [20]. However, the observations show a statistically significant excess over the secondary background. The extra antimatter could be coming from other places. One idea is that nearby pulsars accelerate electrons and positrons to high energies and release them into space [22]. Another possibility is connected to dark matter. If dark matter particles can annihilate or decay, they could hypothetically create antimatter [23, 24].

Detecting antimatter in cosmic rays is not an easy task. The signals are extremely rare compared to the background of normal matter. A single antiproton can be lost in a sea of millions of protons. To separate them, detectors need to be extremely precise. High-resolution sensors are needed to measure their mass, charge, and energy. The Balloon-borne Experiment with a Superconducting Spectrometer (BESS) [25] and the Alpha Magnetic Spectrometer (AMS) [26, 27, 28] were built to do exactly this. Their task is to observe the rare antiparticles hidden in the background and measure their properties in detail. The results they have provided are among the most accurate so far, and they are a key step toward figuring out where cosmic antimatter comes from.

3.1 Experimental results on antimatter abundance in cosmic rays

3.1.1 Alpha Magnetic Spectrometer (AMS)

The Alpha Magnetic Spectrometer (AMS), shown on Fig. 3.1 [26], is a particle detector that has been mounted on the International Space Station (ISS) since May 2011 [29]. It was built to study cosmic rays with high precision. The main goals are to search for signs of primordial antimatter, look for possible evidence of dark matter, and measure the composition and energy of cosmic rays [26]. AMS distinguishes particles from antiparticles by measuring their charge, momentum, and energy. This makes it possible to identify rare events, such as positrons [28, 29] or even heavier antinuclei [30]. Operating in space removes the effects of the atmosphere and allows measurements over a wide range of energies [31]. For antimatter

studies, AMS is important because it gives direct measurements of antiparticles in cosmic rays and reports precise fluxes. When no events are observed, it instead provides stringent upper limits on those fluxes.[27, 29]. More than ten years after its launch, it is still in orbit and continues to expand our knowledge of high-energy particles in the universe [32].

Figure 3.1: AMS mounted on the ISS, tilted 12° from zenith to avoid the rotating solar arrays, and designed to operate for the Station's lifetime [26].

Experimental overview and principle of operation

The AMS-02 detector consists of several subsystems that together allow the identification of cosmic-ray particles and antiparticles. A schematic view of the experiment with the role of each component is given in Fig. 3.2.

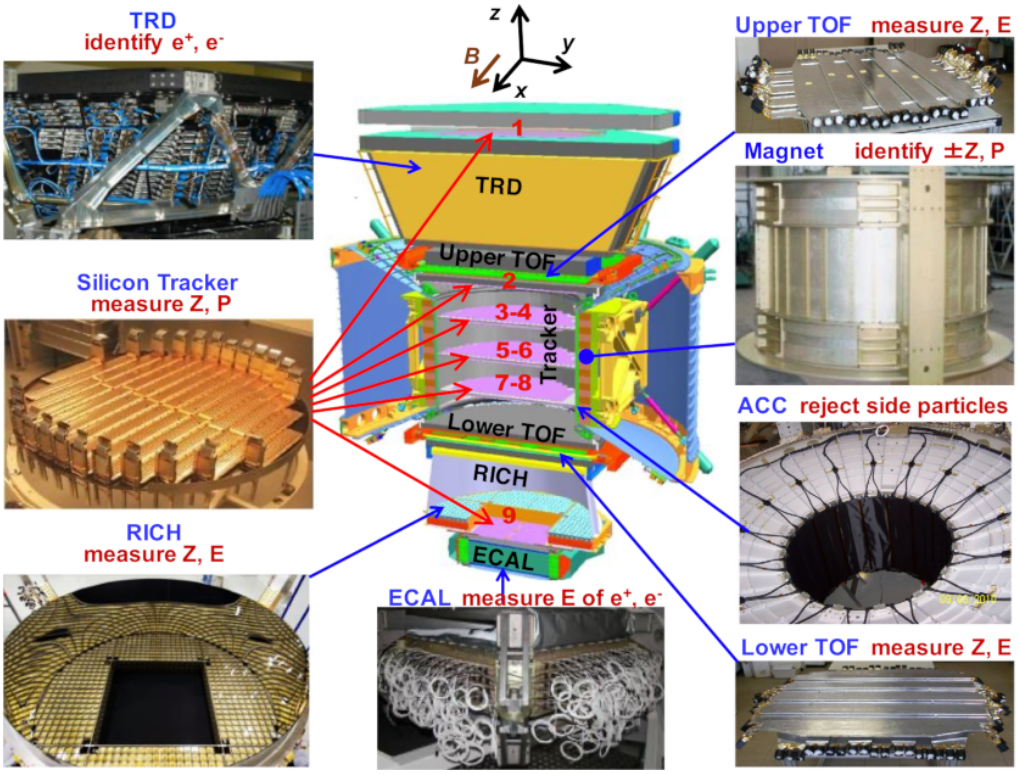

Figure 3.2: Schematic view of the AMS-02 spectrometer for the ISS [33]. Its principle of operation relies on bending of charged particle trajectories in a magnetic field, tracking their positions, and measuring their timing, velocity, and energy [26].

- Permanent Magnet

  The AMS-02 spectrometer uses a permanent magnet, that produces a field of about 0.14 T. The magnet is roughly 0.8 m long with an inner bore of about 1.1 m. The permanent-magnet geometry and measured field are shown in Fig. 3.3. Its yoke and return-field geometry minimize the external dipole moment (leakage field) [26]. In this field, charged particles follow curved trajectories. The orientation of the curvature distinguishes matter from antimatter as they bend in opposite directions. The detector records their positions along the way with a nine-layer silicon tracker.

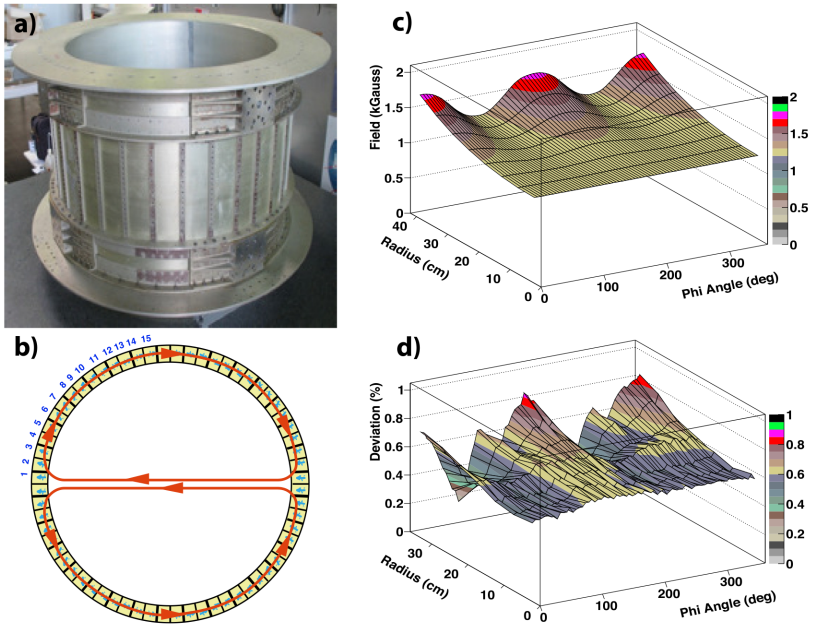

Figure 3.3: (a) AMS magnet in preparation for the ISS; length 800 mm, inner diameter 1115 mm. (b) Layout of the 64-sector permanent magnet, whose opposing field directions yield a negligible net dipole and minimal external leakage. (c) Magnetic field measured in 2010 at $z = 0$. (d) Difference between the 1997 and 2010 field measurements. Radius R and azimuth ϕ are cylindrical coordinates in the x-y plane, with $\phi = 0$ along the x-axis [26].

- Silicon Tracker

  The silicon tracker is made up of nine double-sided layers, as shown in Fig. 3.4. These layers follow the particle's path very precisely and also measure |Z| from the amount of energy it loses when passing through. The tracker is adjusted in orbit to keep its alignment stable to within a few microns. That stability is important for keeping the measurements of rigidity and charge sign accurate over a long period of time. Together, the magnet and tracker are the main tools for measuring a particle's momentum, differentiating between e^+ and e^-, and measuring its nuclear charge [26].

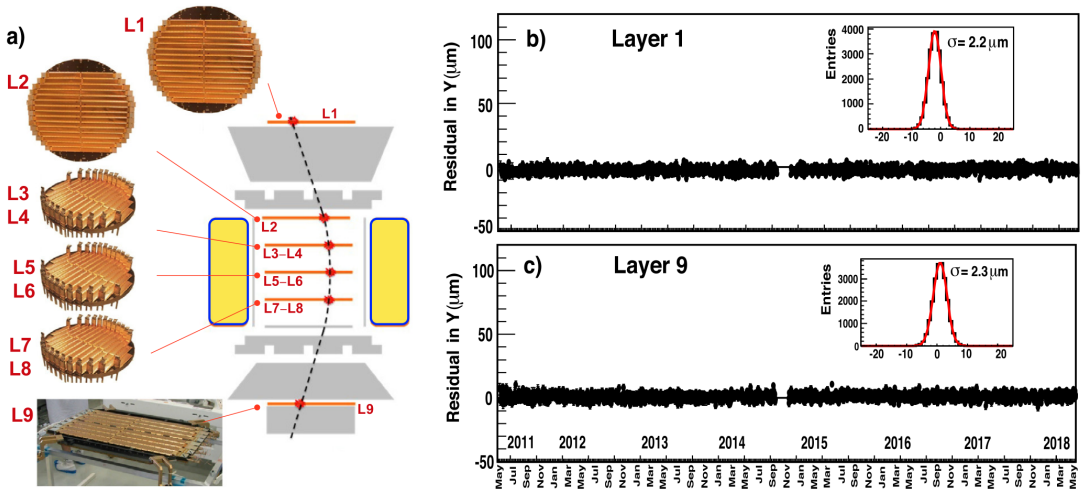

Figure 3.4: (a) The 9 layers of the AMS silicon tracker and their locations within the detector. The alignment stability of (b) Layer 1 and (c) Layer 9 over seven years [26].

- Time of Flight counters(TOF)

  The TOF system measures the flight time between its upper and lower planes. From this measurement AMS obtains the particle's velocity. The TOF also provides the direction of travel (distinguishing downward from upward going particles) and an independent charge estimate via the energy loss dE/dx in the scintillators [34]. TOF information is used early in event selection to confirm a relativistic particle and to reject albedo or events with incorrect timing. Its timing also ties the subdetectors together during reconstruction [34, 35]. Over seven years of operation, the TOF maintained stable performance. The average time resolution is about 160 ps for $Z = 1$ particles [26]. It improves with increasing charge, reaching about 50 ps for $Z > 6$. This corresponds to a velocity resolution of $\Delta(1/\beta) \approx 4\%$ for $Z = 1$, 2% for $Z = 2$, and 1% for $Z > 6$ [26].

- Transition Radiation Detector (TRD)

  The TRD is designed to differentiate electrons and positrons from protons by detecting transition radiation, which is produced when very fast leptons cross layers of different materials. In AMS, it consists of many straw tubes arranged in layers, with radiators placed in between. As a particle passes through, the TRD measures signals in these tubes and builds a likelihood that it is a lepton rather than a proton. The detector was designed for stable, low-power operation in space and reads out thousands of straws with a recirculating gas system. In analysis, TRD information is combined with the Electromagnetic Calorimeter (ECAL) shower shape and tracker variables to achieve strong proton rejection [36, 37].

- Ring-Imaging Cherenkov Detector (RICH)

  The RICH measures a particle's velocity (β) by detecting the Cherenkov light it emits when passing through a transparent radiator at a speed greater than the speed of light in that medium. In AMS-02, this radiator is made from aerogel tiles, chosen for their low refractive index, which allows precise velocity measurements over a wide range of particle energies. Photons produced in the radiator are reflected and focused onto an array of photomultiplier tubes. Their pattern forms a ring whose radius depends on β [38, 26]. By combining this velocity measurement with the rigidity from the tracker, AMS-02 can determine the particle's mass, enabling separation of different isotopes in the GeV

per nucleon range. The RICH also measures the particle's charge with high precision, which is especially important for heavier nuclei. In addition, it provides consistency checks for the velocity measured by the TOF and improves lepton–hadron separation in certain analyses [38]. A schematic of the RICH, the reflector and photodetector plane, and the velocity/charge resolution curves for the aerogel radiator are shown in Fig. 3.5.

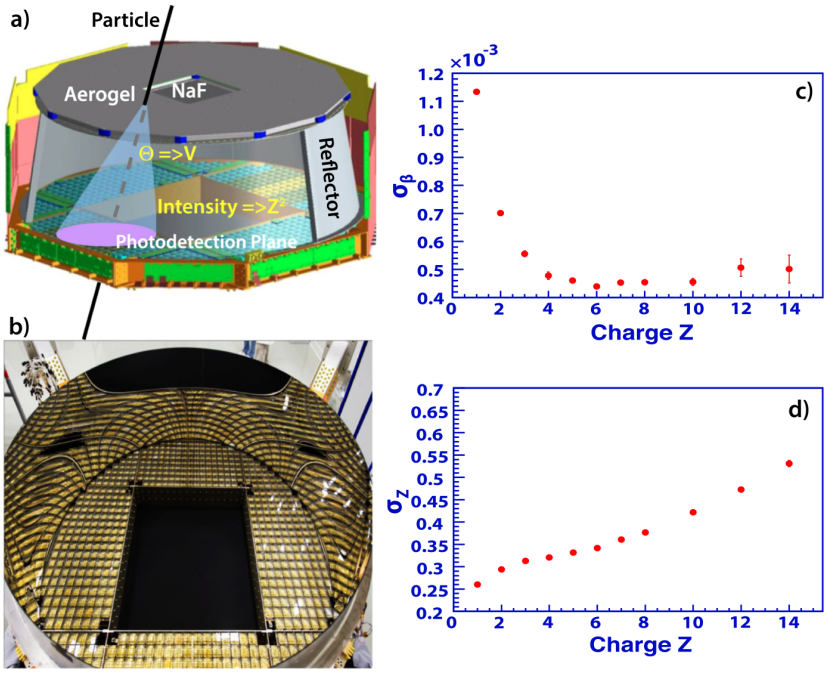

Figure 3.5: (a) RICH schematic; (b) reflector and photodetector plane; (c) velocity and (d) charge resolutions versus charge Z for the aerogel radiator [26].

- Electromagnetic Calorimeter (ECAL)

  The Electromagnetic Calorimeter (ECAL) measures the energy of electrons, positrons, and photons by recording the showers they create when interacting with the detector material. It is a sampling calorimeter built in a shashlik configuration, made from alternating layers of lead and scintillating fibers [39, 37]. The calorimeter has 9 superlayers, each composed of lead foils interleaved with bundles of scintillating fibers. The orientation of the fibers alternates by 90° from one superlayer to the next, which allows the three-dimensional reconstruction of the shower profile [26]. As a particle enters the ECAL, it initiates a cascade of secondary particles. The light produced in the fibers is read out to reconstruct the shower in three dimensions. The calorimeter is deep enough (17 radiation lengths) to fully contain electromagnetic showers for electrons and positrons over a wide range of energies [37]. By analyzing the shape and spread of the shower, the ECAL can distinguish electromagnetic particles from hadrons such as protons. It also provides directional information, which helps confirm the event geometry [26].

Selected Results from the AMS experiment

The AMS-02 detector has provided highly precise measurements of the main antimatter components in cosmic rays. Three key results could be obtained: the positron fraction and spectra, the antiproton flux and ratio, and the time-dependent variations that become important at lower rigidities. These observations give the most reliable evidence so far about

possible sources of antimatter in our galaxy [26]. Before reaching AMS-02, the cosmic rays pass through the heliosphere, where the Sun's magnetic field and solar wind can alter their paths and energies. This effect is known as solar modulation and it depends on the charge of the particle. Positive and negative particles are affected differently. AMS-02 daily data clearly shows this charge-sign dependence [32]. If this effect is not properly taken into account, features observed in the spectra may be misinterpreted as originating from astrophysical sources, while in reality they are shaped by the varying conditions of the solar environment [32].

1. **Positron Fraction**

   One of the most surprising outcomes from AMS-02 has to do with positrons in cosmic rays. To study them, the experiment looks at what is called the positron fraction - the number of positrons compared to the total amount of electrons plus positrons e^+ $/(e^- + e^+)$ [28].

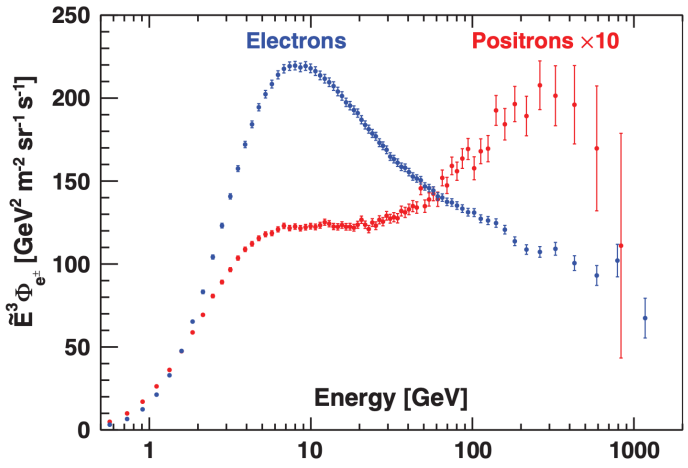

Figure 3.6: AMS-02 measured electron and positron fluxes (scaled as $E^3\Phi$) versus energy. Positron data (×10) show hardening above 20 GeV, extending to TeV energies. The red data points highlight positrons and the blue data points highlight the electrons [40].

At first, one would expect the positron fraction to drop smoothly as the energy goes up. That is what the usual astrophysical models predict [20]. Looking at Fig. 3.6 and Fig. 3.7, it is clear that the AMS-02 data does not follow that rule. Instead, starting around 10 GeV, the fraction rises and keeps increasing up to about 300 GeV. This is surprising because such a steady rise is not something the standard sources of cosmic rays, like supernova remnants, can explain. It points to the idea that there must be other sources in the Galaxy producing extra positrons. Something beyond the normal secondary production where cosmic rays hit interstellar matter. Above 300 GeV, the fraction no longer rises but seems to flatten out, even smoothly decrease. The exact reason for this is still unclear. The shape of the curve already gives useful information about which explanations are possible and which are less likely. Another surprising point is that there is no sudden drop in the spectrum, at least not up to the highest energies measured so far by AMS-02, which reach nearly 1 TeV [28, 29].

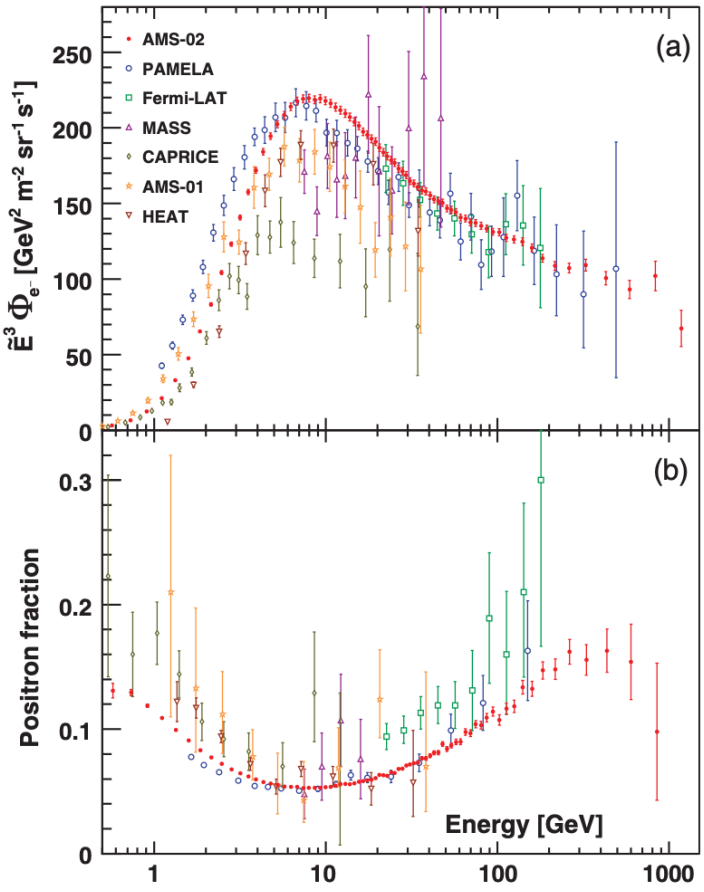

Figure 3.7: (a) AMS-02 electron spectrum ($\tilde{E}^3\Phi_{e^-}$), shown as red data points plotted at $\tilde{E}$. (b) AMS-02 positron fraction (red data points, positioned at bin centers). Comparisons are made with earlier measurements from PAMELA [41], Fermi-LAT [42], MASS [43], CAPRICE [44], AMS-01 [45], and HEAT [46, 47, 48, 41].

There are a few ideas about why the positron fraction behaves this way. One possibility is that nearby astrophysical sources, such as pulsars, are producing and accelerating electron-positron pairs. They later add to the cosmic ray flux we measure. Another idea is that dark matter particles, if they exist and can annihilate or decay, could generate positrons with energy patterns similar to what AMS-02 has observed. At the moment, most studies point to pulsars as a likely explanation for a large part of the excess, though this alone might not cover all the details in the data. The dark matter scenario is still considered possible, but testing it properly will require even more accurate measurements, especially at the highest energies [22].

2. **Antiproton Flux and Ratio Measurements**

   AMS-02 has measured the antiproton–to–proton ($\bar{p}/p$) ratio in cosmic rays with extreme precision, from about 1 GV up to 450 GV [40]. Daily proton flux variations over solar cycle 24 are shown in Fig 3.8.

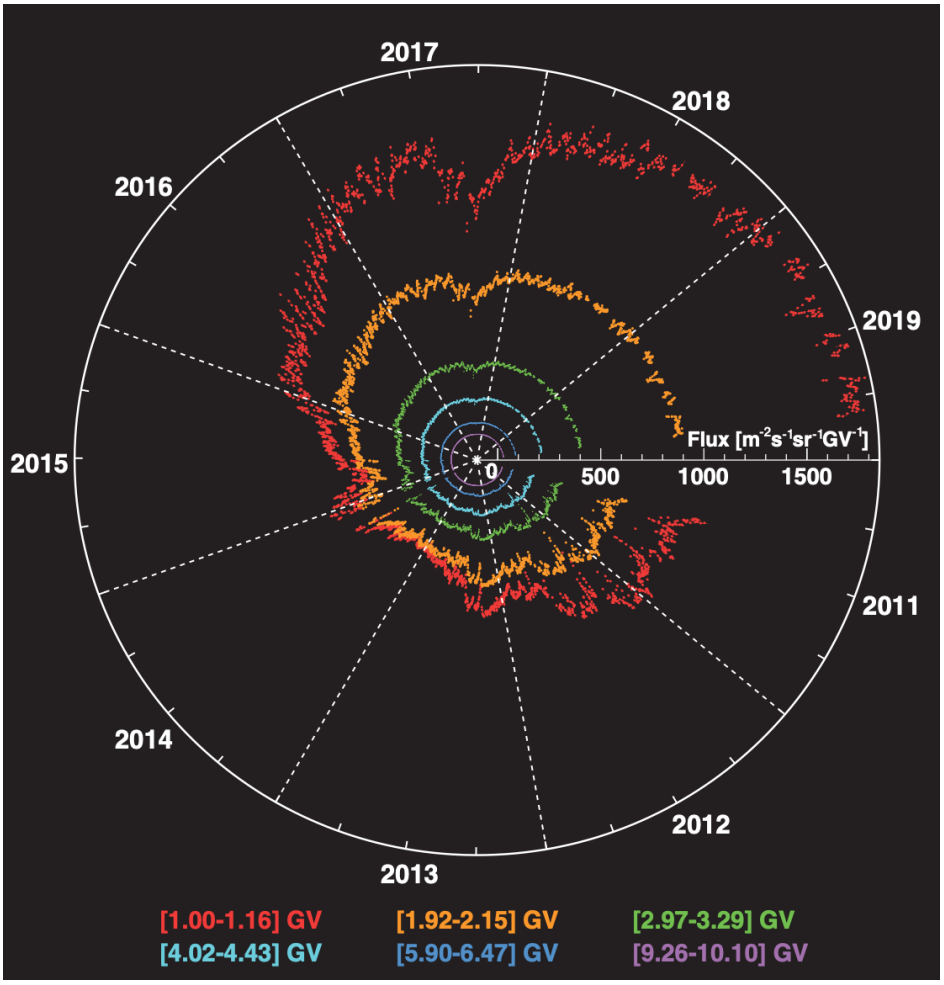

Figure 3.8: Daily AMS proton fluxes are shown for six rigidity bins between 1.00 and 10.10 GV, measured from May 2011 to October 2019. This period covers most of solar cycle 24, including its rise, peak, and decline. For the two lowest bins, days affected by solar energetic particle events (SEPs) were removed. The small gaps in the data come from times when the detector was undergoing checks or upgrades. Error bars are too small to be visible. The flux clearly changes over time, with stronger variations at low rigidities and smaller variations as rigidity increases [40].

The presented data coincide with standard cosmic-ray models at rigidities below $\sim 100GV$. According to these models, antiprotons are secondary products, produced when primary cosmic-ray protons collide with interstellar gas [20]. The accuracy of the measurements, with uncertainties of about 3%, strongly agrees with the models of cosmic-ray propagation through the galaxy [27]. Above $\sim 100GV$ the situation changes. The ratio shows a persistent excess of antiprotons compared to what models predict, about 20% higher. The effect is statistically significant. The fact that it has appeared in every AMS-02 data release so far [27], and matches earlier results from PAMELA [31], or even predictions from exotic sources such as evaporating primordial black holes [49], makes it very unlikely that this is just an instrumental problem or solar modulation. Furthermore, models invoking dark matter annihilation or decay remain viable explanations [24].

Looking ahead, AMS-02 is expected to keep running for the rest of the decade. With more statistics and a higher rigidity reach, future measurements may finally show whether the excess is a genuine sign of new physics or simply an indication that our

models of cosmic-ray transport still need to be refined [26].

3. **Search for Antihelium Nuclei**

   The AMS-02 experiment has conducted the most sensitive search to date for antihelium nuclei in cosmic rays. After analyzing data collected over more than a decade of operation, no confirmed antihelium events have been detected [30]. This null result places an upper limits on the possible abundance of antihelium in cosmic rays. The current limit stands at less than 1.1 antihelium nuclei per million helium nuclei, with 95% confidence level [30].

3.1.2 BESS (Balloon-borne Experiment with a Superconducting Spectrometer)

BESS (Balloon-borne Experiment with a Superconducting Spectrometer) is a Japan–US project that studies cosmic rays. Its main goals are to look for antimatter and to measure the energy and intensity of the light cosmic-ray components. Low-energy antiprotons are a key target. If BESS were to see more low-energy antiprotons than standard secondary production predicts, it could point to sources such as primordial black holes or other dark-matter-related processes. BESS also searches for antihelium. Finding even one antihelium nucleus would have major consequences for cosmology and particle physics, including the question of whether the Universe contains large regions of antimatter. In addition, BESS measures light elements to improve models of cosmic-ray transport and to support atmospheric neutrino flux calculations [25].

Experimental overview

Since 1993, BESS has completed nine successful balloon flights, upgrading the instrument over time. The spectrometer uses a thin-wall superconducting solenoid, time-of-flight (TOF) scintillator hodoscopes, inner drift chambers (IDC), a jet-type drift tracking chamber, and an aerogel Cherenkov counter (which replaced the outer drift chambers used in early flights). The components are arranged in a horizontal cylindrical layout, with the IDC and JET chambers inside the warm bore of the magnet to keep material along the particle path low [50].

The BESS-Polar payload configuration is shown in Fig. 3.9. It represents a cylindrical magnetic spectrometer flown on a long-duration balloon. It includes a thin superconducting solenoid ($\sim$ 0.8 T), a jet-type drift chamber with inner drift chambers for tracking, top/middle/bottom time-of-flight hodoscopes, and a silica-aerogel Cherenkov counter. The tracker sits inside the magnet bore to reduce material. Momentum is measured from track curvature. The TOF system measures the particle's flight time between the upper and lower scintillator planes; with the known distance, this gives the velocity $\beta = v/c$. The aerogel counter rejects electron and muon backgrounds. The payload is powered by a solar array beneath the spectrometer. The instrument and DAQ drew about 460 W during flight [51].

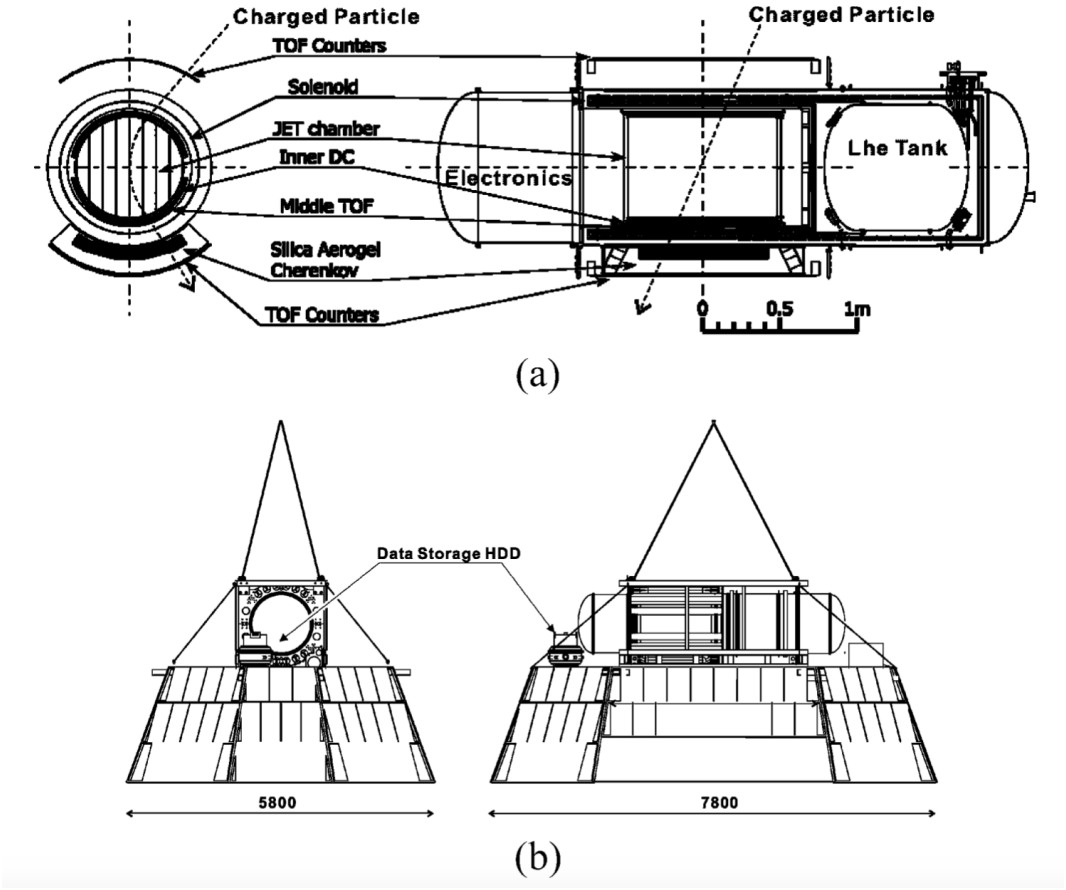

Figure 3.9: Configuration of the BESS-Polar spectrometer for balloon flight: (a) spectrometer layout with TOF counters, solenoid, inner and JET drift chambers, middle TOF, and aerogel Cherenkov; (b) whole payload with developed solar cells [51].

The solenoid, shown in Fig. 3.10, is ultra-thin and built without an outer support cylinder by using high-strength aluminum-stabilized superconductor. It is designed to keep the material budget very low. [51]. The coil diameter is about 0.9 m, its length about 1.4 m, and the coil thickness about 3.5 mm, with a mass of roughly 40 kg [51]. The cryostat uses a double vacuum wall with two radiation shields, and the detector region totals about $2.5\,\mathrm{g\,cm^{-2}}$ of material [51]. The magnet operates in persistent-current mode in flight; the current can be dumped through a 0.15 Ωresistor, and a back-pressure regulator keeps the helium evaporation stable during ascent and float [51].

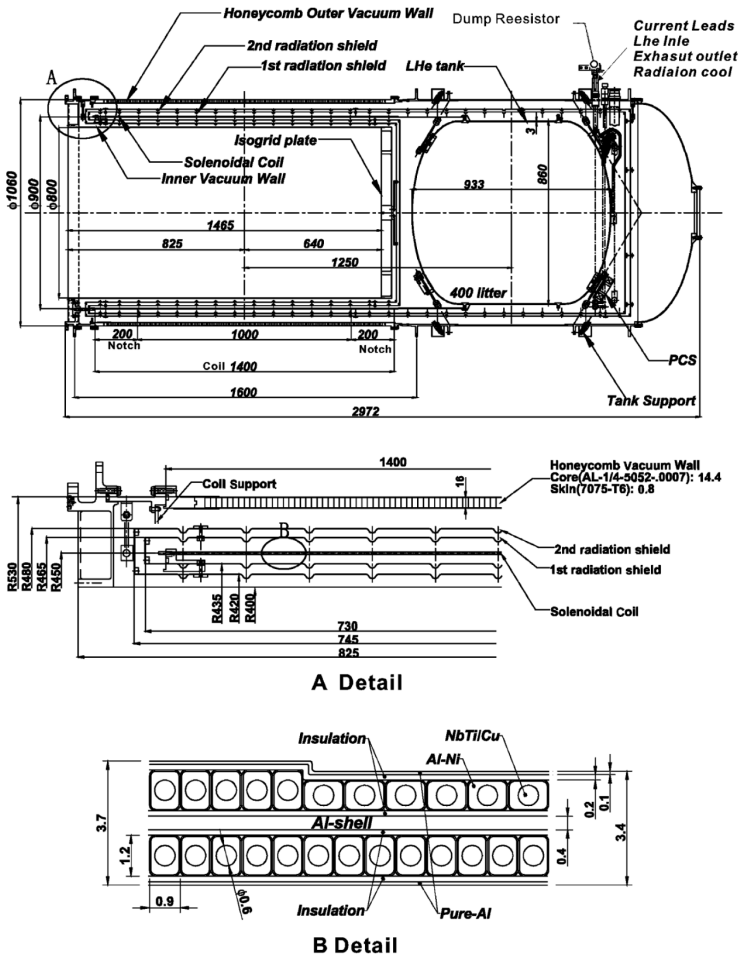

Figure 3.10: Cross-sectional views of the BESS-Polar solenoid magnet and cryostat, showing the coil, radiation shields, double vacuum walls, and the 400 L liquid-helium tank [51].

The current version, BESS-Polar, keeps the same basic design but is a new build with an ultra-thin KEK superconducting magnet. This minimizes material and extends sensitivity to the lowest antiproton energies. BESS-Polar has the largest geometry factor among balloon-borne magnetic spectrometers and is optimized for studies of Z=1 and Z=2 components (antiprotons and antihelium). The plan at the time was a first flight from McMurdo in December 2004, followed by a second flight near the 2007 solar minimum. Thanks to long-duration flights, higher event efficiency, and the low geomagnetic cutoff, BESS-Polar was expected to improve low-energy antiproton statistics by more than a factor of 20 over previous data [50].

Principle of operation

BESS-Polar as shown in Fig. 3.11, identifies antimatter using three measurements as a particle passes through the instrument: its speed, the way it bends in a magnetic field, and whether it produces Cherenkov light. A particle from above first hits the time-of-flight (TOF) counters on the top and then the middle or bottom. From the travel time and the known path length, BESS gets the velocity β and the flight direction. The inner drift chambers then record many hit points while the particle moves through the solenoidal field ($\sim$0.8 T). The curve of the track gives the rigidity $R \equiv pc/(Ze)$ and the sign of the charge from the bend direction. If we combine R with β, we can differ heavy, slow particles from light, fast ones.

Last, the aerogel Cherenkov counter ($n \sim 1.02$) works as a threshold veto - very fast particles make Cherenkov light, while slower ones do not [52, 51].

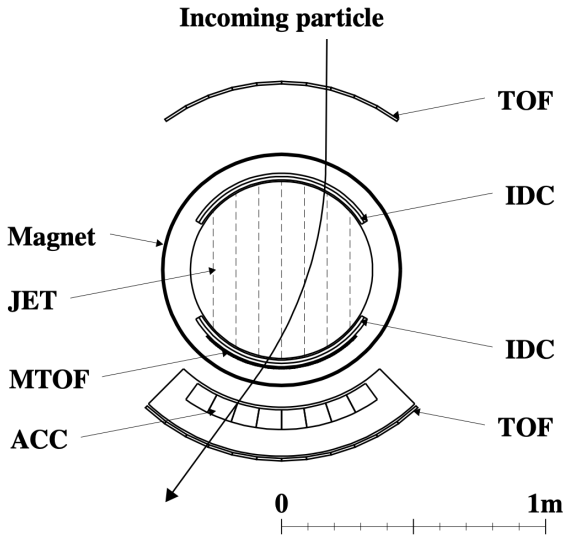

Figure 3.11: Cross-sectional views, showing the principle of a particle passing through, showcasing the way the magnet field deflects the charged particles. [52]

In case the particle is an electron. It is almost at the speed of light, so TOF gives $\beta \approx 1$. It also makes Cherenkov light in the aerogel. Even though its curvature is negative (like an antiproton), the "too fast" β and the Cherenkov signal mark it as an electron/muon. We reject it [52].

If the particle is an antiproton, it is a bit more tricky. Its curvature is negative, but it is slower than an electron at the same momentum. TOF says $\beta < 1$. The mass from R and β matches a proton-mass particle with $Z = 1$. Below about $4\,\mathrm{GeV}/c$ it does not make Cherenkov light, so it passes the veto. That gives a clean antiproton sample in the BESS-Polar range [52].

For antihelium, the idea is the same but with $|Z| = 2$. We look for negative curvature, charge magnitude 2, and β consistent with a heavy nucleus. BESS has found no antihelium. Only the upper limits are reported [53].

Results

In the following part, we summarize the BESS–Polar measurements that are most relevant to the antimatter search in the universe.

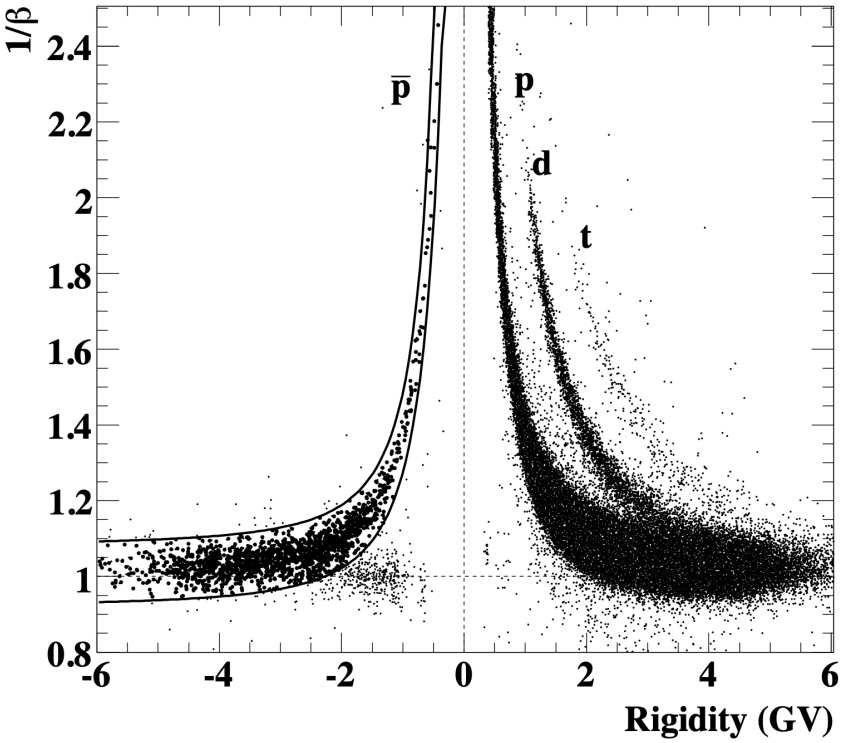

Figure 3.12: $1/\beta$ vs. rigidity $R \equiv pc/(Ze)$. When $R < 0$ the particle has negative charge, so real antiprotons make a thin band along the heavy $Z = 1$ line. Electrons and muons are mostly removed by the aerogel Cherenkov veto, and only 0.5% of positive-R points are shown to keep the plot clear [52].

Fig. 3.12 demonstrates how BESS identifies antiprotons. The vertical axis shows $1/\beta$ (inverse speed), while the horizontal axis shows rigidity $R \equiv pc/(Ze)$. Points with negative R correspond to negatively charged particles. Antiprotons appear in this negative-R region when genuine. The solid band indicates the allowed parameter space for antiprotons, where $1/\beta$ values match expectations for a heavy $Z = 1$ particle at each rigidity. Events outside this band are rejected. On the positive-R side, protons (p), deuterons (d), and tritons (t) are visible and labeled. Antiproton candidates are represented by slightly larger dots for better visibility. Only a small random subset (0.5%) of positive-R events is displayed to prevent overcrowding. Prior to this selection, BESS eliminates most electron and muon backgrounds using the aerogel Cherenkov veto, which explains the absence of a dense electron band. The final result is a distinct, narrow strip of antiproton candidates in the negative-R region, representing the core identification process [52].

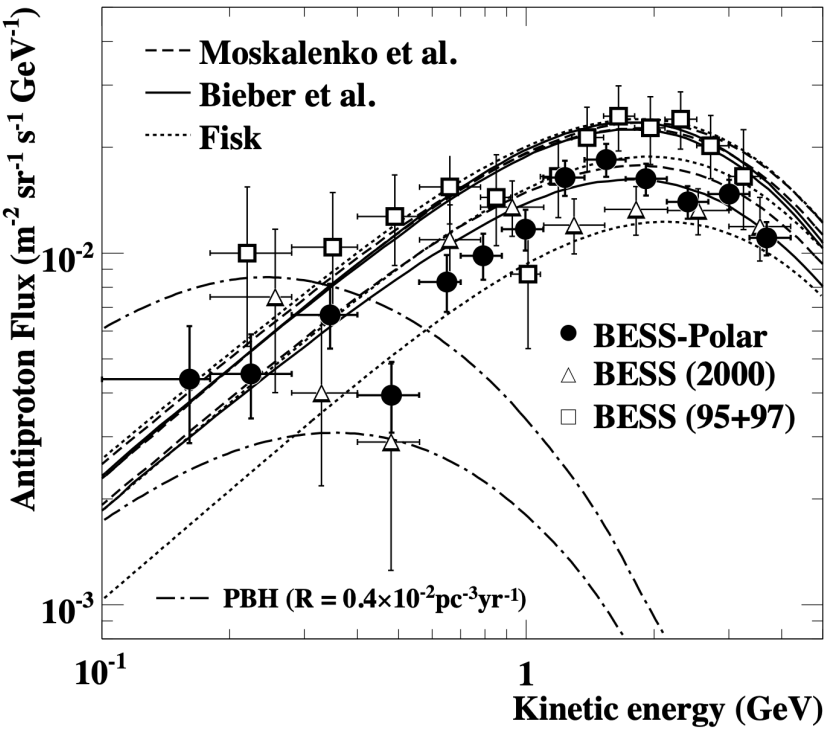

Figure 3.13: Antiproton flux at the top of the atmosphere vs. kinetic energy. It peaks near 2 GeV and is well described by secondary-production models. The lines show different transport and solar-modulation choices, and the dash–dot line is a possible PBH source [52].

Fig. 3.13 gives the measured antiproton flux versus kinetic energy. The black circles are BESS-Polar I (the 2004 Antarctic flight). The triangles and squares show earlier BESS flights (1995+1997 and 2000). The dashed, solid, and dotted curves are model predictions. They include different ways of treating transport in the Galaxy and solar modulation near Earth. The dash-dot curves are an example of an extra source: antiprotons from evaporating primordial black holes (PBH). The BESS-Polar I spectrum runs from about 0.1 to 4.2 GeV and peaks near $\sim$2 GeV. That "bump" is expected for secondary production and transport. Across most of the range, the BESS-Polar I points follow the standard secondary-production models within errors. The PBH curves would lift the lowest-energy region. The data do not require that extra component. This tells us that, in this energy band and solar phase, antiprotons look compatible with secondaries [52].

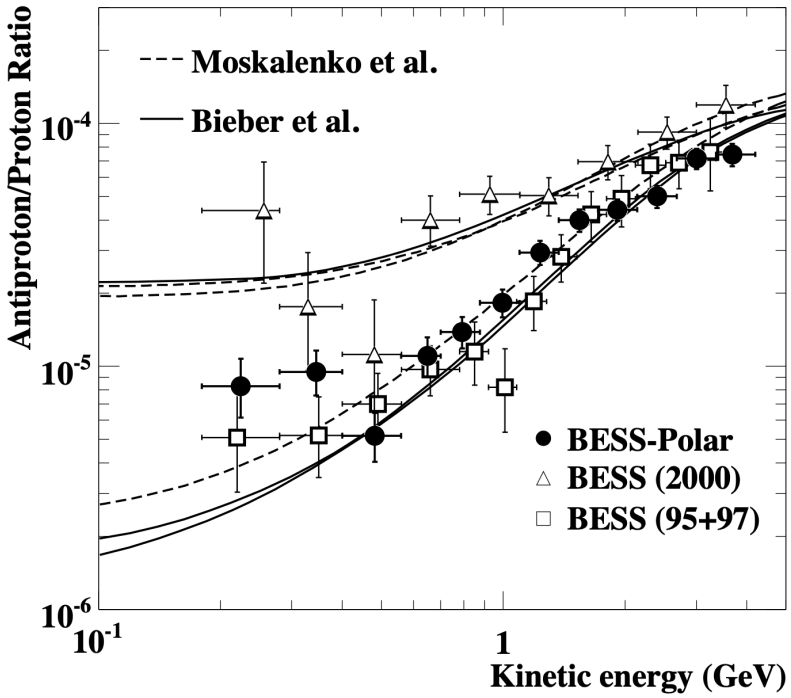

Figure 3.14: Antiproton/proton ratio vs. energy. The BESS–Polar I points match the "secondary" models, so no extra source is needed. Small shifts between years come from solar activity [52].

In Fig. 3.14, the vertical axis is the antiproton–to–proton ratio ($\bar{p}/p$). BESS–Polar I appears as black circles, with previous BESS results and model predictions shown for comparison. The ratio rises from $\sim 10^{-6}$ at a few hundred MeV to $\sim 10^{-4}$ at a few GeV. That rise comes from the production threshold and how transport and solar modulation affect opposite charges. BESS-Polar I sits on the model bands within uncertainties. This plot is useful because many systematic effects cancel in the ratio. It also shows the impact of the solar cycle. Basically, measurements taken in different years shift a bit, and the drift-modulation models track those shifts. The take-home message is that BESS-Polar I supports a secondary origin for antiprotons in this range, with no need for an additional primary source [52].

Chapter 4

Indirect information on the presence antimatter - INTEGRAL mission

The International Gamma-Ray Astrophysics Laboratory (INTEGRAL), shown on Fig. 4.1, was launched by the European Space Agency in October 2002 [54]. It was sent into an elliptical orbit. This kind of orbit was chosen because it lets the satellite stay far from the Earth's radiation belts for a long period of time. This secures low background and long uninterrupted observations can be made [54]. Its main goal is to study the universe in gamma rays, but also in X-rays and optical light at the same time [54].

As gamma rays cannot be studied directly from the ground due to the Earth's atmosphere [55], INTEGRAL was designed to answer several questions, some of them being How are heavy elements created in stars and supernovae? What powers compact objects like black holes and neutron stars? Where does the antimatter in our Galaxy come from[21, 56]? To answer these, INTEGRAL carries four different instruments, which are mounted together and observe the same region of sky. These are SPI, IBIS, JEM-X and OMC [57, 58, 59, 54]. Together they cover energies from a few keV up to about 10 MeV [54].

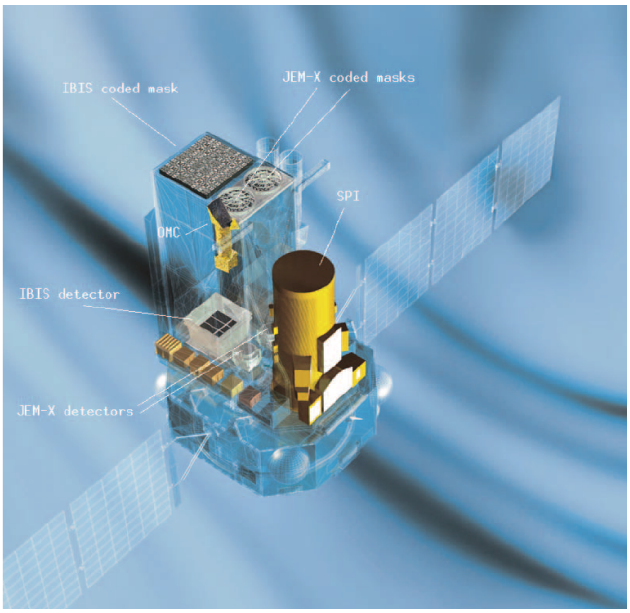

Figure 4.1: Schematic view of the INTEGRAL spacecraft with the four instruments mounted on it [54].

4.1 Experimental overview

4.1.1 SPectrometer on INTEGRAL (SPI)

The Spectrometer on INTEGRAL (SPI), as shown in Fig. 4.2, is the key INTEGRAL instrument for antimatter studies [60, 21]. It provides high-resolution γ-ray spectroscopy over ($\sim$20 keV–8 MeV) [54]. Its core is an array of 19 high-purity germanium (HPGe) detectors in a hexagonal layout, cryogenically cooled to about 85 K to deliver an energy resolution of roughly2 keV to 3 keV at 511 keV [57, 56, 60]. Cooling is provided by Stirling-cycle mechanical cryocoolers together with a passive radiator and cold finger coupled to the cryostat [54].

Above the detector array sits a $\sim$3 cm-thick tungsten *coded-aperture* mask with a pseudo-random pattern of open and closed cells [54]. A coded mask is a plate that selectively blocks or transmits incoming γ rays in a known pattern, so each sky direction imprints a distinct "shadowgram" on the detector plane. The sky image is then recovered by mathematically deconvolving the recorded shadow with the known mask pattern [55]. SPI uses this technique to reconstruct images while operating at energies where focusing optics are ineffective. The approach naturally defines fully- and partially-coded fields of view with highest sensitivity in the fully-coded region [54, 55]. A BGO (bismuth germanate) anti-coincidence shield surrounds the detectors. It covers the sides, top, and bottom with collimator rings, side shields, and a base shield. It detects photons and particles that do not come through the mask. When the shield is triggered, the event in the detectors is vetoed. This reduces the instrumental and cosmic-ray background by more than 90% [54]. At the very top, SPI has a thin plastic scintillator veto (PSAC), 5 mm thick. It rejects charged particles that might come straight through the aperture and mimic a gamma ray [54]. The detectors sit inside a beryllium cryostat, passively cooled to about 210 K. The point is to thermally isolate the HPGe array so leakage currents stay low and the energy resolution stays stable; the active Stirling machines then bring the Ge crystals down to operating temperature ($\sim$85 K). This cryostat setup keeps the detectors stable during long exposures in orbit [54, 60].

When a 511 keV photon from electron–positron annihilation arrives from the sky, it first encounters the coded mask. Depending on its direction, it either passes through one of the open holes or is absorbed in the tungsten. In the first case, it enters one of the germanium detectors. Inside the crystal, the photon deposits its energy via photoelectric absorption or Compton scattering. This energy creates electron–hole pairs that are collected as an electrical pulse. The amplitude of the pulse is proportional to the photon energy, and the front-end electronics of the system (FEE) can record it with keV precision [61]. If the photon comes from outside the coded aperture, or if it is caused by a cosmic-ray interaction, the BGO shield triggers and vetoes the event. In this way, only photons that come through the aperture are kept. By accumulating many events, SPI generates a spectrum of the incoming radiation. When annihilation occurs, a sharp peak at 511 keV appears in the spectrum, together with a continuum from positronium formation [56, 57]. By repeating this process while pointing at different directions, SPI collects many different shadowgrams. From these, a map of the sky in 511 keV radiation is reconstructed. This is how SPI produced the first detailed maps of positron annihilation in the Milky Way [62, 60].

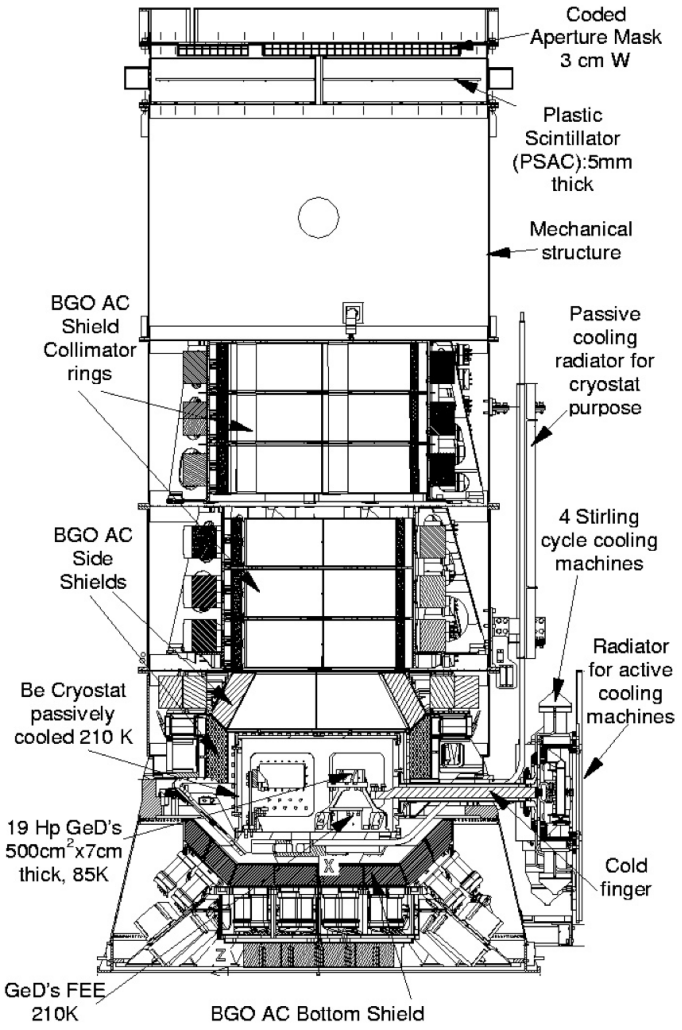

Figure 4.2: Cut-out view of the SPI spectrometer, showing mask, plastic scintillator, passive radiator, BGO anti-coincidence shield, germanium detector array, cold finger, and cooling machines [63].

4.1.2 Imager on Board the Integral Satellite (IBIS)

The IBIS imager, shown in Fig. 4.3, is the second large instrument [64]. It is built for sharp images of the sky in the hard X-ray and soft gamma-ray band. IBIS has two layers of detectors. The top layer, ISGRI, is made of CdTe semiconductor pixels and is sensitive from 15 keV up to about 1 MeV. The bottom layer, PICsIT, is made of CsI scintillators and works at higher energies, up to about 10 MeV. The two layers can also be used in coincidence, which allows IBIS to detect Compton scattering events and to measure photon directions in another way. The coded mask of IBIS is thicker and sits higher above the detectors compared to SPI. The angular resolution is much better, about 12 arcminutes, which makes IBIS useful for distinguishing crowded fields and identifying point sources [64]. For the study of antimatter, IBIS has been used to search for point-like emitters of the 511 keV line. So far no compact sources have been detected, which suggests the emission is diffuse [58].

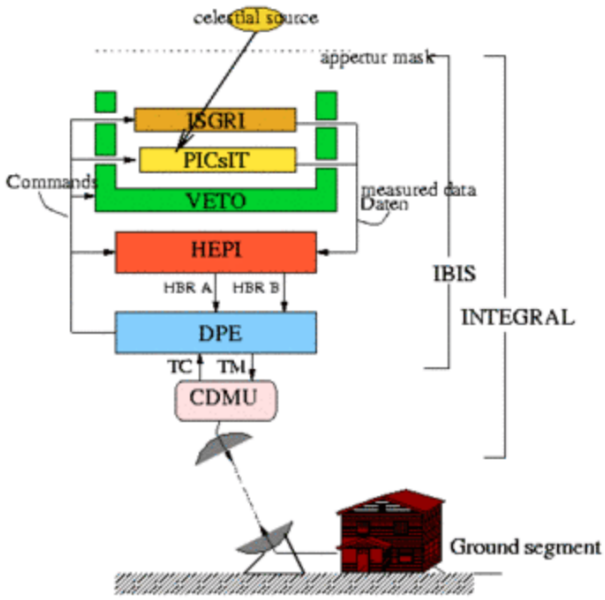

Figure 4.3: Block diagram of the IBIS imager on INTEGRAL. Incoming photons pass through the coded mask and are detected in ISGRI or PICsIT, with background rejection by the veto system. Data are processed onboard and sent to the ground segment for analysis [65].

4.1.3 Joint European X-Ray Monitor (JEM-X)

The JEM-X instrument is the X-ray monitor of INTEGRAL [59]. It consists of two identical telescopes that observe in the energy range between 3 and 35 keV [59]. Each telescope uses a coded mask made of tungsten, placed above a microstrip gas chamber detector. When an incoming X-ray photon passes through the mask and enters the detector, it ionizes the gas inside, and the released charge is collected as an electric signal. In this way both the energy and the position of the photon can be measured. The angular resolution of JEM-X is about $3'$ [59], much sharper than that of SPI. The fully coded field of view is 4.8° in diameter, while the partially coded field extends to 10° [59]. These characteristics make JEM-X well suited for observations of crowded fields, such as the Galactic bulge, where it can identify the active X-ray sources that may also contribute to the high-energy emission detected by SPI and IBIS [59].

4.1.4 Optical Monitoring Camera (OMC)

The Optical Monitoring Camera (OMC) provides optical data for the same fields observed by the high-energy instruments [66]. OMC is a refractive telescope with a 50 mm aperture and a focal length of 154 mm [66]. The detector is a large frame-transfer CCD, operating with a Johnson-V filter centered at 550 nm [66]. The field of view is $5° \times 5°$, which allows OMC to monitor bright stars, novae, and active galactic nuclei in parallel with the gamma-ray and X-ray observations [66]. Its primary data product is V-band light curves (time-series photometry) [66]. The physical connection between emission in different energy bands can be studied by comparing these optical variations with the X-ray and gamma-ray behaviour seen by JEM-X, IBIS, and SPI [66].

4.2 Results

One of the key discoveries of INTEGRAL is the detailed measurement of the 511 keV annihilation line in the Milky Way. Before INTEGRAL, measurements from balloon experiments already hinted at its presence, but INTEGRAL provided the first high-quality maps and spectra [56]. The SPI spectrometer on INTEGRAL has provided the most detailed observations of the Galactic 511 keV annihilation line. Early analyses reported a bulge flux with a line width of roughly 3 keV FWHM [56]. Later work, based on more than ten years of SPI data, confirmed a total bulge flux of around $9.9 \times 10^{-4}\,\mathrm{ph\,cm^{-2}\,s^{-1}}$, with a line width of 2 keV to 3 keV [60]. The spatial distribution is extended across about 8–10° around the Galactic Centre, consistent with a bulge-shaped component [62, 60]. Fig. 4.4 illustrates Sky exposure map for the analyzed SPI data set in 2005 and Fig.4.5 shows the sky exposure map in 2016.

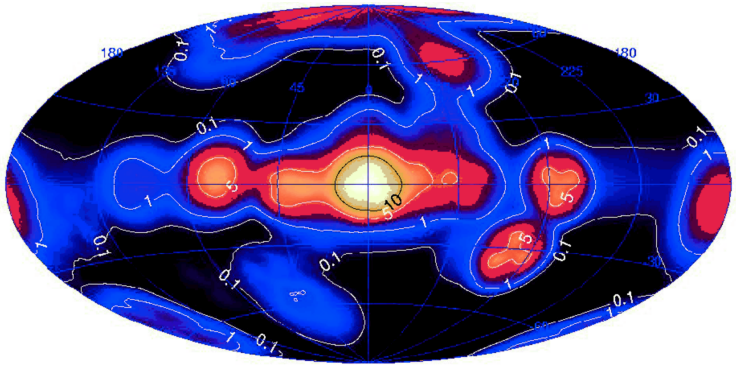

Figure 4.4: SPI map of the 511 keV emission showing the bright bulge and faint disk in 2005 [62].

The spectrum of the bulge, given by Fig. 4.6, and measured by SPI shows a very narrow 511 keV line together with a broad continuum from positronium formation. This indicates that most positrons do not annihilate immediately but slow down in the interstellar medium before they interact. The positronium fraction is high, which points to annihilation occurring in warm or even cold phases of the interstellar gas [60]. To test whether discrete sources could explain the signal, the IBIS imager was used. IBIS has better angular resolution than SPI and is sensitive to point-like emitters. Fig. 4.7 displays the exposure map taken from IBIS. A deep all-sky survey based on more than five years of data and about 10 Ms exposure near the Galactic centre found no point sources at 511 keV [58]. The analysis set a strict 2σ upper limit of $1.6 \times 10^{-4}\,\mathrm{ph\,cm^{-2}\,s^{-1}}$ for individual sources in the central region. This absence of detections means that no single object, such as a microquasar or an X-ray binary, can be the dominant contributor to the bulge emission. Instead, positrons must be created in various sources and then travel through the interstellar medium before annihilation [58].

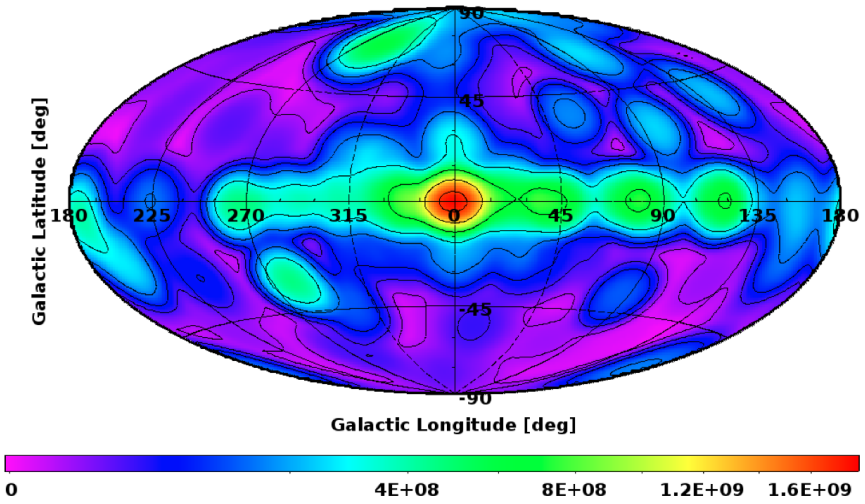

Figure 4.5: Sky exposure map for the analyzed SPI data set. The map units are given in cm^2 s. The contours indicate specific exposure levels, beginning with the innermost contour at 22 Ms and progressing outwards to 16 Ms, 9 Ms, 4 Ms, 2 Ms, 1 Ms, 0.5 Ms, and finally 0.1 Ms. The map is from 2016 [60].

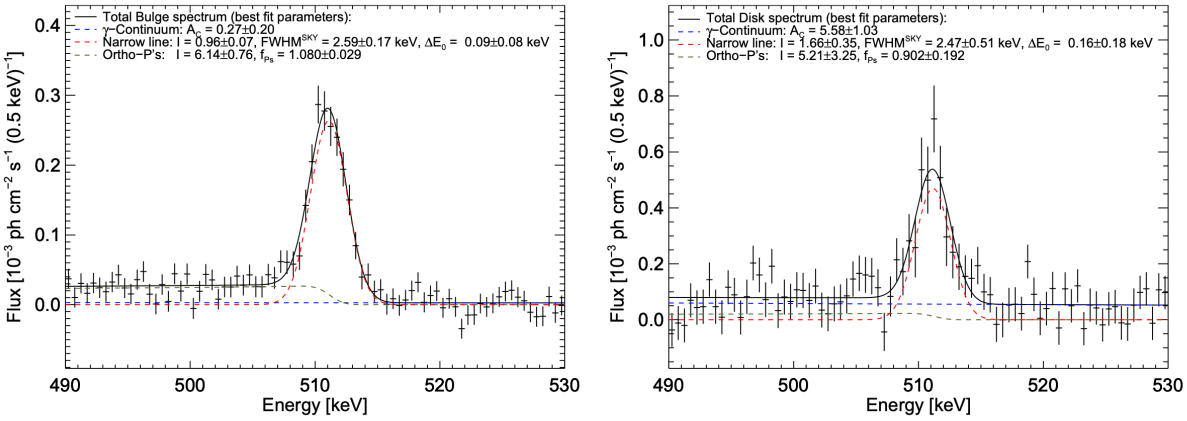

(a) Bulge. (b) Disk.

Figure 4.6: Spectrum of the annihilation gamma-rays from the Galactic bulge (a) and disk (b). The best-fit model (solid black line) is decomposed into its individual components: the 511 keV positron annihilation line (dashed red), the continuum from ortho-positronium annihilation (dashed olive), and the underlying diffuse gamma-ray continuum (dashed blue). The corresponding fitted and derived parameters are provided in the legends [60].

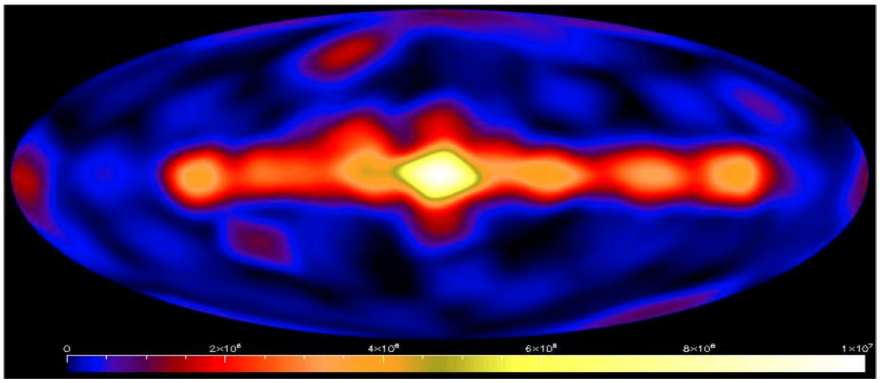

Figure 4.7: Exposure map for the IBIS 511 keV data set. The deepest exposures correspond to the Galactic plane and Galactic centre, where a total exposure of 10 Ms was reached. [58] [60].

The INTEGRAL mission has given the most detailed picture of positron annihilation in the Galaxy. The key result is that the 511 keV line is brightest in the bulge, while the disk is much weaker [62, 60]. This pattern has been confirmed in later studies and reviews, so it is now considered a stable result [67]. The reason for the bulge to be so strong is still unclear. Most of the expected sources of positrons, such as supernovae or pulsars, are distributed along the disk, not the bulge. Either there are hidden bulge sources, or positrons created in the disk are able to travel very far before they annihilate [60, 67]. Both possibilities are difficult to prove with the contemporary data. Different explanations have been proposed. Radioactive isotopes from Type Ia supernovae release positrons in their decay chains, and they are often seen as one of the best explanations [21]. Pulsars and microquasars can also make positrons, although it is not certain if their numbers are enough [67]. There are also more exotic ideas, for example the possibility of dark matter particles producing positrons, but this remains speculative [21]. Before INTEGRAL, the 511 keV line had been detected by balloon flights and smaller satellite missions, but those measurements were limited and gave inconsistent results [56]. INTEGRAL changed this situation. With long observing times, high energy resolution, and wide coverage of the sky, it made possible both a reliable map of the emission and precise spectra [60]. The annihilation line proves that large amounts of antimatter exist in the Milky Way. At the same time, it is still unknown where most of the positrons come from or how they move through the interstellar medium. This is why the 511 keV signal remains one of the most baffling features in astrophysics today [67].

Chapter 5

Measurement of O(1 MeV) gamma rays with nanosatelites

The well-known 511 keV line is produced when electrons and positrons annihilate at rest. But not all annihilations occur this way. If positrons annihilate while moving, the result can be gamma rays that extend into the MeV range [60].

Other processes in astrophysics also give signals in this energy band. Nuclear de-excitation, pion decay, and secondary products of cosmic-ray collisions all create gamma rays around MeV energies. For this reason, instruments that are sensitive to $\mathcal{O}$(1MeV) gamma rays are essential if we want to explore the possible presence of antimatter in the Universe.

5.1 Concept of the Compton Telescope

The detection of such gamma rays in space requires instruments that are compact, efficient, and strong enough to operate under the severe constraints of a nanosatellite. Instead of big observatories, the design relies on compact detectors that use little power but can still measure both the energy and direction of incoming photons through Compton scattering [68].

The idea of a Compton telescope is simple. A gamma photon first scatters in one detector layer and is absorbed in another. From the deposited energies and the hit positions, the direction of the photon can be traced back to a "Compton cone." Combining a large amount of such cones makes it possible to reconstruct an image of the sky. This approach works especially well in the MeV range, where neither pair production nor photo-absorption dominate [55]. For the success of such telescopes, two things are critical: the scintillator material, which must provide fast timing, high light yield, and good resolution; The photon sensor technology, which must remain compact, stable, and low-power in space. Inorganic scintillators have become crucial for future Compton telescopes in the MeV range. Among them, $CeBr_3$ has shown particularly favorable properties. It combines a high light yield of around $6.8 \times 10^4\,\mathrm{ph\,MeV^{-1}}$, a fast decay constant of about 17 ns, and an energy resolution near 4% at 662 keV [69, 70]. This makes it a strong compromise between performance and practicality for compact space-based detectors. A further advantage of $CeBr_3$ is that, unlike $LaBr_3$:Ce, it does not exhibit intrinsic radioactivity. While $LaBr_3$:Ce offers excellent resolution, the natural presence of ^{138}La produces background events that complicate measurements in low-noise conditions such as space [71]. For this reason, $CeBr_3$ is considered a more suitable option for nanosatellites and low-background astrophysical applications.

For studying of the position reconstruction with monolithic $CeBr_3$ crystal and segmented photodetector array, a small-scale Compton telescope prototype was constructed with two $CeBr_3$ crystals of different thicknesses, each coupled to segmented SiPM arrays. The Compton

telescope's experimental components are shown in Fig. 5.1. Before mounting the Back end and the Front end together, the subsystems were tested to establish calibration and working conditions. The response was linear across the gamma lines used (^{22}Na, ^{137}Cs, ^{60}Co), which fixed the energy scale. Increasing the SiPM bias improved the energy resolution up to an optimal value, after which dark noise became noticeable. The thicker $CeBr_3$ crystal provided higher full-energy peak efficiency, while the thinner crystal gave slightly better resolution, so the two were assigned to roles consistent with stopping power and scattering. These results set the final settings used in the prototype. [72]

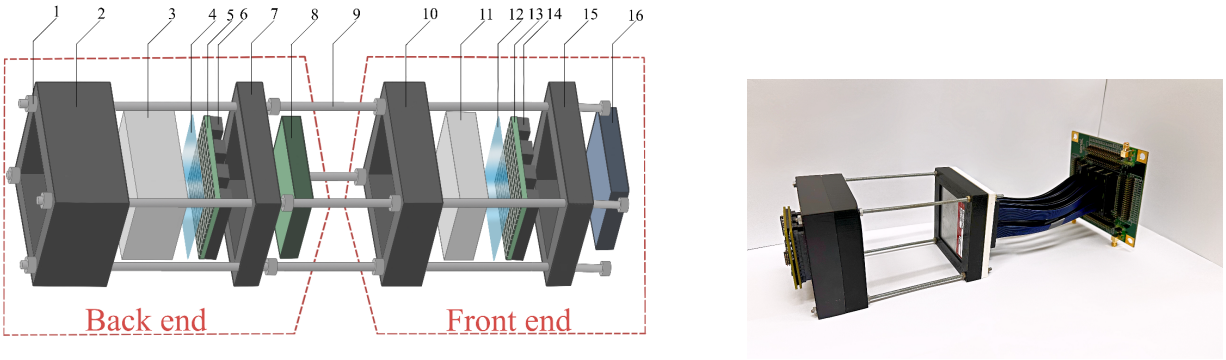

(a) Schematic representation with labeled components.

(b) Assembled Compton telescope.

Figure 5.1: Compton-telescope prototype. (a) Schematic with components: 1—Fasteners; 2—3D-printed upper casing for the thick crystal; 3—$CeBr_3$ thick scintillator crystal; 4—silicone optical grease; 5—SiPM matrix; 6—Samtec 80-way connectors (QTE-040-03-F-D-A); 7—3D-printed lower casing; 8—AiT AB424T-ARRAY144P tileable 4+24-channel hybrid active base; 9—metal rod; 10—3D-printed upper casing for the thin crystal; 11—$CeBr_3$ thin scintillator crystal; 12—silicone optical grease; 13—SiPM matrix; 14—Samtec 80-way connectors (QTE-040-03-F-D-A); 15—3D-printed lower casing; 16—ARRAYC-30035-144P breakout board. (b) Assembled instrument.

Incident γ rays first Compton scatter in the thin $CeBr_3$ front module and are then absorbed in the thick $CeBr_3$ back module. Each crystal is coupled to a segmented SiPM matrix; row and column sums are routed to 32-channel receiver–preamplifier boards and a power/slow-control module. A constant-fraction discriminator (CFD) forms single-module triggers from the summed signals, and a logic unit builds a coincidence to define valid events. On a valid trigger, the V1742 digitizer records the selected channels, while rates and slow-control parameters (HV/LV, T, V, I) are monitored. Data are transferred to the DAQ PC via optical link, as shown in Fig. 5.2).

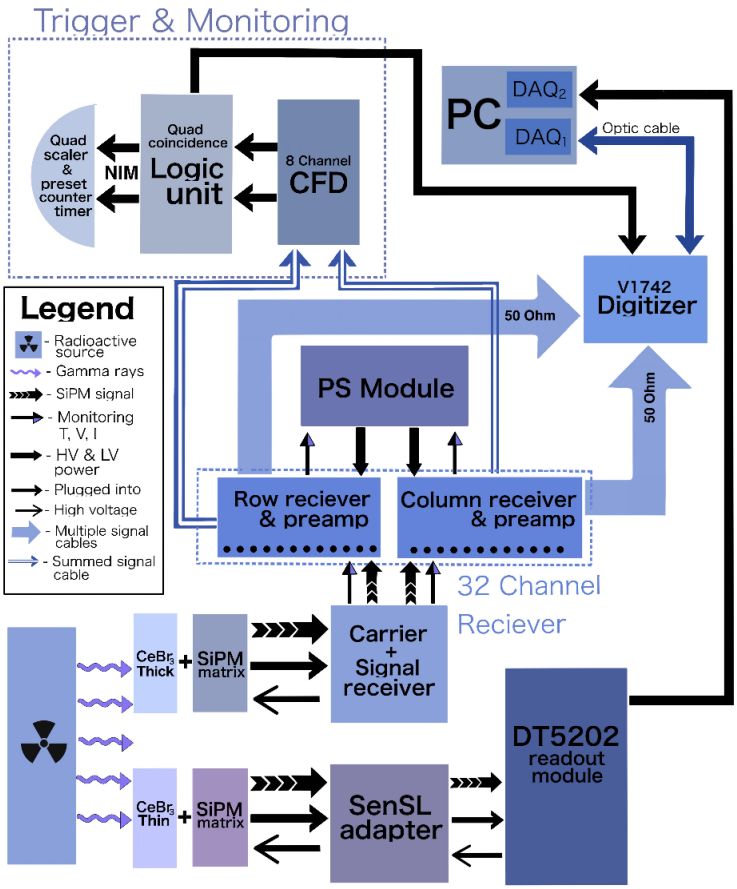

Figure 5.2: Block scheme of the Experimental setup

.

Monte Carlo studies showed that such a configuration is capable of reconstructing Compton scattering events with energy, within the expected region, and angular resolution. The setup was highly modular, low-power, and built with compact readout systems. The Monte Carlo results demonstrated the trade-off between efficiency and angular acceptance when varying the distance between scatterer and absorber. At 5 cm spacing, the efficiency was $\epsilon = 0.45$ with a field of view of about 1 sr, while at 10 cm spacing the efficiency dropped to $\epsilon = 0.40$ with a narrower field of view. Thus, compact geometries are favorable for maximizing detection in a limited payload volume. Another important result was that events involving 180° scattering between detectors gave the best energy and time resolution, suggesting that even small telescopes can achieve competitive reconstruction quality if optimized properly. Using compact $CeBr_3$ scintillators together with SiPM arrays offers a clear solution. $CeBr_3$ gives high light output, fast response, and good energy resolution [69]. SiPMs also bring clear benefits over photomultiplier tubes. They are small, need low voltage, and are more robust for space instruments [73]. These features fit well with CubeSat limits in size and power. Tests of Compton telescope prototypes confirm that even small, modular systems can reach good efficiency and angular resolution.

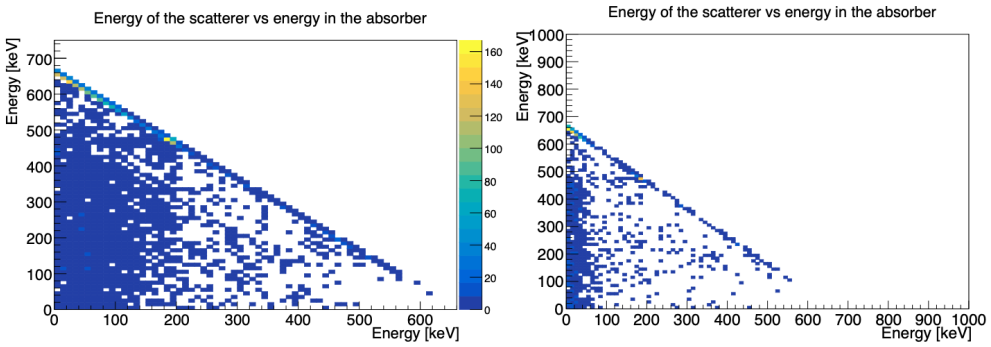

Figure 5.3: Monte Carlo distributions of energy deposits in the scatterer vs absorber. The horizontal axis is the energy deposited in the absorber E_2 and the vertical axis is the energy deposited in the scatterer E_1 (fully contained events satisfy $E_1 + E_2 \approx 662\,\text{keV}$). Left: plane separation 5 cm; right: 10 cm.

.

Chapter 6

Conclusions

Antimatter has been studied for almost a century, ever since Dirac's theory predicted its existence and Anderson later confirmed it with the discovery of the positron. Its presence in nature is now beyond doubt, but the question of why the Universe is dominated by matter remains unanswered. According to the SM, matter and antimatter should have been produced in equal amounts after the Big Bang. If that were the case, the two would have annihilated almost completely. Clearly, that did not happen, and the reason for this imbalance is still unknown. One explanation involves CP violation. This phenomenon shows that matter and antimatter do not always behave in the same way. It was first observed in kaon decays and later in other systems as well. Still, the size of the effect measured so far is too small to explain the matter–antimatter asymmetry. This makes it clear that additional processes, possibly beyond the SM, must be involved. Experimental results provide strong input to this discussion. The AMS experiment on the ISS has measured positrons and antiprotons in cosmic rays with very high precision. Many of the results follow the expectations from secondary production, but some features indicate that other sources, such as pulsars or even dark matter, could play a role. The BESS experiment has complemented these discoveries at lower energies. It has also searched for anti-helium, but no signal has been observed. This supports the view that large regions of antimatter do not exist in our observable Universe. INTEGRAL has added another important result by mapping the 511 keV annihilation line in the Milky Way. Its data confirm that positrons are present in large numbers, especially in the Galactic bulge. The exact source of these positrons is not yet identified. They may come from known astrophysical processes such as supernovae and compact objects, but explanations that involve more exotic physics cannot be ruled out. Future research will need both theory and new technology. On the theoretical side, models of baryogenesis and CP violation must be extended to account for the asymmetry. On the experimental side, new detector designs are being developed. Small gamma-ray telescopes with SiPM arrays and fast scintillators like $CeBr_3$ can be mounted on nanosatellites. These lightweight instruments could provide valuable data in the MeV energy range and help test the existing models in ways that current experiments cannot. New detector technologies will soon extend these studies. Step by step, physics is moving closer to answering why the Universe is made of matter rather than antimatter.

Bibliography

[1] Paul A. M. Dirac. The quantum theory of the electron. *Proc. Roy. Soc. Lond. A*, 117:610–624, 1928. doi:10.1098/rspa.1928.0023.

[2] Carl D. Anderson. The positive electron. *Science*, 76(1967):238–239, 1932.

[3] Albert Einstein. On the electrodynamics of moving bodies. *Annalen Phys.*, 17:891–921, 1905. doi:10.1002/andp.200590006.

[4] The story of antimatter | timeline.web.cern.ch — timeline.web.cern.ch. https://timeline.web.cern.ch/timeline-header/86. [Accessed 25-08-2025].

[5] David J. Griffiths. *Introduction to Elementary Particles*. Wiley-VCH, 2nd edition, 2008. URL: https://cds.cern.ch/record/111880.

[6] James D Bjorken et al. *Relativistic quantum mechanics*. International series in pure and applied physics. McGraw-Hill, New York, NY, 1964. URL: https://cds.cern.ch/record/100769.

[7] Richard Phillips Feynman. The theory of positrons. *Physical Review*, 76:749–759, 1949. doi:10.1103/PhysRev.76.749.

[8] I. J. R. Aitchison and A. J. G. Hey. *Gauge Theories in Particle Physics*. CRC Press, 4 edition, 2013.

[9] Frank Close. *Antimatter*. Oxford University Press, Oxford, UK, 2009.

[10] Eugene D. Commins and Philip H. Bucksbaum. *Weak Interactions of Leptons and Quarks*. Cambridge University Press, Cambridge, UK, 1983.

[11] Antonio Pich. The standard model of electroweak interactions, 2012. URL: https://arxiv.org/abs/1201.0537, arXiv:1201.0537.

[12] C. S. Wu et al. Experimental test of parity conservation in beta decay. *Physical Review*, 105:1413–1414, 1957. doi:10.1103/PhysRev.105.1413.

[13] J. H. Christenson et al. Evidence for the 2π Decay of the K_2^0 Meson. *Phys. Rev. Lett.*, 13:138–140, 1964. doi:10.1103/PhysRevLett.13.138.

[14] Val L. Fitch. The discovery of charge-conjugation parity asymmetry. *Rev. Mod. Phys.*, 53:367–371, Jul 1981. URL: https://link.aps.org/doi/10.1103/RevModPhys.53.367, doi:10.1103/RevModPhys.53.367.

[15] Michael Gronau. Cp violation in b meson decays. *Nuclear Physics B - Proceedings Supplements*, 142:263–270, May 2005. URL: http://dx.doi.org/10.1016/j.nuclphysbps.2005.01.047, doi:10.1016/j.nuclphysbps.2005.01.047.

[16] Makoto Kobayashi and Toshihide Maskawa. CP Violation in the Renormalizable Theory of Weak Interaction. *Prog. Theor. Phys.*, 49:652–657, 1973. doi:10.1143/PTP.49.652.

[17] R. L. Workman et al. Review of Particle Physics. *PTEP*, 2022:083C01, 2022. doi:10.1093/ptep/ptac097.

[18] A. D. Sakharov. Violation of CP Invariance, C asymmetry, and baryon asymmetry of the universe. *Pisma Zh. Eksp. Teor. Fiz.*, 5:32–35, 1967. doi:10.1070/PU1991v034n05ABEH002497.

[19] Paul Langacker. Grand unified theories and proton decay. *Physics Reports*, 72(4):185–385, June 1981. doi:10.1016/0370-1573(81)90059-4.

[20] I. V. Moskalenko and A. W. Strong. Production and propagation of cosmic-ray positrons and electrons. *The Astrophysical Journal*, 493(2):694–707, February 1998. doi:10.1086/305152.

[21] N. Prantzos et al. The 511 kev emission from positron annihilation in the galaxy. *Reviews of Modern Physics*, 83(3):1001–1056, September 2011. URL: http://dx.doi.org/10.1103/RevModPhys.83.1001, doi:10.1103/revmodphys.83.1001.

[22] Dan Hooper et al. Pulsars as the sources of high energy cosmic ray positrons. *Journal of Cosmology and Astroparticle Physics*, 2009(01):025–025, January 2009. URL: http://dx.doi.org/10.1088/1475-7516/2009/01/025, doi:10.1088/1475-7516/2009/01/025.

[23] Marco Cirelli, Gennaro Corcella, Andi Hektor, Gert Hütsi, Mario Kadastik, Paolo Panci, Martti Raidal, Filippo Sala, and Alessandro Strumia. Pppc 4 dm id: a poor particle physicist cookbook for dark matter indirect detection. *Journal of Cosmology and Astroparticle Physics*, 2011(03):051–051, March 2011. URL: http://dx.doi.org/10.1088/1475-7516/2011/03/051, doi:10.1088/1475-7516/2011/03/051.

[24] Annika Reinert et al. A precision search for wimps with charged cosmic rays. *Journal of Cosmology and Astroparticle Physics*, 2018(01):055–055, January 2018. URL: http://dx.doi.org/10.1088/1475-7516/2018/01/055, doi:10.1088/1475-7516/2018/01/055.

[25] Y. Asaoka et al. Measurements of cosmic-ray low-energy antiproton and proton spectra in a transient period of solar field reversal. *Physical Review Letters*, 88(5), January 2002. URL: http://dx.doi.org/10.1103/PhysRevLett.88.051101, doi:10.1103/physrevlett.88.051101.

[26] M. Aguilar et al. The alpha magnetic spectrometer (ams) on the international space station: Part ii — results from the first seven years. *Physics Reports*, 894:1–116, 2021. URL: https://cds.cern.ch/record/2751454, doi:10.1016/j.physrep.2020.09.003.

[27] M. Aguilar et al. Antiproton Flux, Antiproton-to-Proton Flux Ratio, and Properties of Elementary Particle Fluxes in Primary Cosmic Rays Measured with the Alpha Magnetic Spectrometer on the International Space Station. *Phys. Rev. Lett.*, 117(9):091103, 2016. doi:10.1103/PhysRevLett.117.091103.

[28] L. Accardo et al. High-statistics measurement of the positron fraction in primary cosmic rays of 0.5–500 gev with the alpha magnetic spectrometer on the international space station. *Physical Review Letters*, 113(12):121101, 2014. doi:10.1103/PhysRevLett.113.121101.

[29] M. Aguilar et al. Electron and Positron Fluxes in Primary Cosmic Rays Measured with the Alpha Magnetic Spectrometer on the International Space Station. *Phys. Rev. Lett.*, 113:121102, 2014. doi:10.1103/PhysRevLett.113.121102.

[30] J. Alcaraz and others. Search for antihelium in cosmic rays. *Physics Letters B*, 461(4):387–396, September 1999. URL: http://dx.doi.org/10.1016/S0370-2693(99)00874-6, doi:10.1016/s0370-2693(99)00874-6.

[31] O. Adriani et al. PAMELA Measurements of Cosmic-ray Proton and Helium Spectra. *Science*, 332:69–72, 2011. arXiv:1103.4055, doi:10.1126/science.1199172.

[32] M. Aguilar et al. Temporal Structures in Positron Spectra and Charge-Sign Effects in Galactic Cosmic Rays. *Phys. Rev. Lett.*, 131(15):151002, 2023. doi:10.1103/PhysRevLett.131.151002.

[33] Piergiorgio Picozza and R. Sparvoli. Detection of antimatter in our galaxy. *Journal of Physics: Conference Series*, 203, 01 2010. doi:10.1088/1742-6596/203/1/012021.

[34] D. Casadei and others. The ams-02 time of flight system. *Nuclear Physics B - Proceedings Supplements*, 113(1–3):133–138, December 2002. URL: http://dx.doi.org/10.1016/S0920-5632(02)01832-7, doi:10.1016/s0920-5632(02)01832-7.

[35] V. Bindi et al. Calibration and performance of the AMS-02 time of flight detector in space. *Nucl. Instrum. Meth. A*, 743:22–29, 2014. doi:10.1016/j.nima.2014.01.002.

[36] Thomas Kirn. The AMS-02 TRD on the international space station. *Nucl. Instrum. Meth. A*, 706:43–47, 2013. doi:10.1016/j.nima.2012.05.010.

[37] C. Adloff et al. The AMS-02 lead-scintillating fibres Electromagnetic Calorimeter. *Nucl. Instrum. Meth. A*, 714:147–154, 2013. doi:10.1016/j.nima.2013.02.020.

[38] Luísa Arruda, Fernando Barão, and Rui Pereira. Particle identification with the ams-02 rich detector: D/p and anti-d/anti-p separation, 2008. URL: https://arxiv.org/abs/0801.3243, arXiv:0801.3243.

[39] F. Cadoux et al. The ams-02 electromagnetic calorimeter. *Nuclear Physics B - Proceedings Supplements*, 113(1–3):159–165, 2002. doi:10.1016/S0920-5632(02)01836-4.

[40] M. Aguilar et al. Periodicities in the Daily Proton Fluxes from 2011 to 2019 Measured by the Alpha Magnetic Spectrometer on the International Space Station from 1 to 100 GV. *Phys. Rev. Lett.*, 127(27):271102, 2021. doi:10.1103/PhysRevLett.127.271102.

[41] M Aguilar et al. Towards understanding the origin of cosmic-ray electrons. *Phys. Rev. Lett.*, 122:101101, Mar 2019. URL: https://link.aps.org/doi/10.1103/PhysRevLett.122.101101, doi:10.1103/PhysRevLett.122.101101.

[42] M. Ackermann et al. Measurement of separate cosmic-ray electron and positron spectra with the fermi large area telescope. *Phys. Rev. Lett.*, 108(1):011103, January 2012. URL: https://link.aps.org/doi/10.1103/PhysRevLett.108.011103, doi:10.1103/PhysRevLett.108.011103.

[43] C. Grimani et al. Measurements of the absolute energy spectra of cosmic-ray positrons and electrons above 7 gev. *Astronomy & Astrophysics*, 392(1):287–294, 2002. doi:10.1051/0004-6361:20020845.

[44] M. Boezio et al. The cosmic-ray electron and positron spectra measured at 1 au during solar minimum activity. *Advances in Space Research*, 27(4):669–674, 2001. doi:10.1016/S0273-1177(01)00112-8.

[45] M. Aguilar and others. Cosmic-ray positron fraction measurement from 1 to 30 gev with ams-01. *Physics Letters B*, 646:145–154, 2007. doi:10.1016/j.physletb.2007.01.024.

[46] S. W. Barwick and others. Measurements of the cosmic-ray positron fraction from 1 to 50 gev. *Astrophysical Journal*, 498:779–789, 1998.

[47] M. A. DuVernois and others. Cosmic-ray electrons and positrons from 1 to 100 gev: Measurements with heat and their interpretation. *Astrophysical Journal*, 559:296–303, 2001.

[48] J. J. Beatty and others. New measurement of the cosmic-ray positron fraction from 5 to 15 gev. *Physical Review Letters*, 93:241102, 2004.

[49] Cecilia Lunardini and Yuber F. Perez-Gonzalez. Dirac and majorana neutrino signatures of primordial black holes. *Journal of Cosmology and Astroparticle Physics*, 2020(08):014–014, August 2020. URL: http://dx.doi.org/10.1088/1475-7516/2020/08/014, doi:10.1088/1475-7516/2020/08/014.

[50] BESS - Information Page — asd.gsfc.nasa.gov. https://asd.gsfc.nasa.gov/bess/BESS.html. [Accessed 27-08-2025].

[51] Yasuhiro Makida et al. Ballooning of an ultra-thin superconducting solenoid for particle astrophysics in antarctica. *Applied Superconductivity, IEEE Transactions on*, 16:477 – 480, 07 2006. doi:10.1109/TASC.2005.869659.

[52] K. Abe and others. Measurement of the cosmic-ray low-energy antiproton spectrum with the first bess-polar antarctic flight. *Physics Letters B*, 670(2):103–108, December 2008. URL: http://dx.doi.org/10.1016/j.physletb.2008.10.053, doi:10.1016/j.physletb.2008.10.053.

[53] K. Abe et al. Search for antihelium with the bess-polar spectrometer. *Phys. Rev. Lett.*, 108:131301, Mar 2012. URL: https://link.aps.org/doi/10.1103/PhysRevLett.108.131301, doi:10.1103/PhysRevLett.108.131301.

[54] C. Winkler et al. The INTEGRAL mission. *Astron. Astrophys.*, 411:L1–L6, November 2003. doi:10.1051/0004-6361:20031288.

[55] V. Schönfelder. *The Universe in Gamma Rays*. Springer, 2004.

[56] Pierre Jean et al. Early SPI / INTEGRAL measurements of 511 keV line emission from the 4th quadrant of the Galaxy. *Astron. Astrophys.*, 407:L55, 2003. arXiv:astro-ph/0309484, doi:10.1051/0004-6361:20031056.

[57] E. Churazov et al. Positron annihilation spectrum from the galactic centre region observed by spi/integral revisited: annihilation in a cooling ism?: Positron annihilation spectrum from the gc. *Monthly Notices of the Royal Astronomical Society*, 411(3):1727–1743, November 2010. URL: http://dx.doi.org/10.1111/j.1365-2966.2010.17804.x, doi:10.1111/j.1365-2966.2010.17804.x.

[58] G. De Cesare. Searching for the 511 kev annihilation line from galactic compact objects with the ibis gamma ray telescope. *Astronomy /& Astrophysics*, 531:A56, June 2011. URL: http://dx.doi.org/10.1051/0004-6361/201116516, doi:10.1051/0004-6361/201116516.

[59] Niels Lund et al. Jem–x: The x-ray monitor aboard integral. *http://dx.doi.org/10.1051/0004-6361:20031358*, 411, 11 2003. doi:10.1051/0004-6361:20031358.

[60] Thomas Siegert et al. Gamma-ray spectroscopy of positron annihilation in the milky way. *Astronomy /& Astrophysics*, 586:A84, January 2016. URL: http://dx.doi.org/10.1051/0004-6361/201527510, doi:10.1051/0004-6361/201527510.

[61] J.-P. Roques et al. Spi/integral in-flight performance. *Astronomy & Astrophysics*, 411:L91–L100, 2003. doi:10.1051/0004-6361:20031501.

[62] J. Knödlseder and others. The all-sky distribution of 511 kev electron-positron annihilation emission. *Astronomy /& Astrophysics*, 441(2):513–532, September 2005. URL: http://dx.doi.org/10.1051/0004-6361:20042063, doi:10.1051/0004-6361:20042063.

[63] G. Vedrenne et al. Spi: the spectrometer aboard integral. *Astronomy and Astrophysics, vol. 411, no. 1, p. L63-L70*, 411, 11 2003. doi:10.1051/0004-6361:20031482.

[64] P. Ubertini et al. Ibis: The imager on-board integral. *Astronomy & Astrophysics*, 411:L131–L139, 2003. URL: https://www.aanda.org/articles/aa/full/2003/43/aaINTEGRAL13/aaINTEGRAL13.right.html, doi:10.1051/0004-6361:20031224.

[65] University of Tübingen. INTEGRAL/IBIS project page — Astronomy & Astrophysics, University of Tübingen. https://uni-tuebingen.de/en/fakultaeten/mathematisch-naturwissenschaftliche-fakultaet/fachbereiche/physik/institute/astronomie-und-astrophysik/astronomie-hea/forschung/abgeschlossene-projekte/integral-ibis/. [Accessed 28-08-2025].

[66] J. M. Mas-Hesse et al. Omc: An optical monitoring camera for integral. *Astronomy & Astrophysics*, 411:L261–L268, 2003. doi:10.1051/0004-6361:20031418.

[67] Eugene Churazov et al. INTEGRAL results on the electron-positron annihilation radiation and X-ray & Gamma-ray diffuse emission of the Milky Way. *New Astron. Rev.*, 90:101548, November 2020. doi:10.1016/j.newar.2020.101548.

[68] Carolyn A. Kierans et al. The 2016 super pressure balloon flight of the compton spectrometer and imager, 2017. URL: https://arxiv.org/abs/1701.05558, arXiv:1701.05558.

[69] K. S. Shah et al. $CeBr_3$ scintillators for gamma-ray spectroscopy. *IEEE Transactions on Nuclear Science*, 51(5):2395–2399, 2004. doi:10.1109/TNS.2004.835733.

[70] A. J. Workman et al. Characterisation of $cebr_3$ scintillators for future space missions. *Nuclear Instruments and Methods in Physics Research Section A*, 1035:166870, 2022. doi:10.1016/j.nima.2022.166870.

[71] Hao Cheng et al. Intrinsic radioactivity of $labr_3$:ce and $cebr_3$ scintillation crystals. *Journal of Physics: Conference Series*, 1468(1):012233, 2020. doi:10.1088/1742-6596/1468/1/012233.

[72] Veronika Asova et al. Multichannel SiPM test readout system for gamma ray measurements with monolithic inorganic $CeBr_3$. *J. Phys. Conf. Ser.*, 2794(1):012006, 2024. doi:10.1088/1742-6596/2794/1/012006.

[73] N. Otte et al. The potential of sipm as photon detector in astroparticle physics experiments like magic and euso. *Nuclear Instruments and Methods in Physics Research Section A: Accelerators, Spectrometers, Detectors and Associated Equipment*, 545(3):705–715, 2005. doi:10.1016/j.nima.2005.02.011.